Automated Localisation of Focal Ventricular Tachycardia from Simulated Implanted Device Electrograms: A Combined Physics-AI Approach

Sofia Monaci[1*], Karli Gillette[2], Esther Puyol-Antón[1], Ronak Rajani[1], Gernot Plank[2], Andrew P. King[1], Martin Bishop[1]

[1]King's College London, United Kingdom, [2]Medical University of Graz, Austria

Submitted to Journal:
Frontiers in Physiology

Specialty Section:
Computational Physiology and Medicine

Article type:
Original Research Article

Manuscript ID:
682446

Received on:
18 Mar 2021

Revised on:
28 May 2021

Journal website link:
www.frontiersin.org

Conflict of interest statement

The authors declare that the research was conducted in the absence of any commercial or financial relationships that could be construed as a potential conflict of interest

Author contribution statement

The work was primarily led by Sofia Monaci. Karli Gillette and Dr. Esther Puyol-Antón were consulted in the initial coding of lead field computations and CNN structure, respectively. Dr Ronak Rajani provided the CT data used for torso model creation. Prof. Gernot Plank was responsible for developing and providing the reaction-eikonal and lead field packages within CARP. Finally, Dr. Andrew King and Dr. Martin Bishop supervised the project, guiding the study design and providing useful insights and feedback on every aspect of the work (from the modelling side to the localisation pipeline and the CNN algorithms).

Keywords

ventricular tachycardia, Implanted devices, Electrograms, Automated localization, torso modelling, deep learning

Abstract

Word count: 264

Background. Focal ventricular tachycardia (VT) is a life-threating arrhythmia, responsible for high morbidity rates and sudden cardiac death (SCD). Radiofrequency ablation is the only curative therapy against incessant VT; however, its success is dependent upon accurate localisation of its source, which is highly invasive and time-consuming.
Objective. The goal of our study is, as a proof-of-concept, demonstrating the possibility of utilising electrograms (EGM) recordings from cardiac implantable electronic devices (CIEDs). To achieve this, we utilise fast and accurate whole torso electrophysiological (EP) simulations in conjunction with convolutional neural networks (CNNs) to automate the localisation of focal VTs using simulated EGMs.
Methods. A highly detailed 3D torso model was used to simulate ~4000 focal VTs, evenly distributed across the left ventricle (LV), utilising a rapid reaction-eikonal environment. Solutions were subsequently combined with lead field computations on the torso to derive accurate electrocardiograms (ECG) and EGM traces, which were used as inputs to CNNs to localise focal sources. We compared the localisation performance of a previously developed CNN architecture (Cartesian probability-based) with our novel CNN algorithm utilising universal ventricular coordinates (UVCs).
Results. Implanted device EGMs successfully localised VT sources with localisation error (8.74mm) comparable to ECG-based localisation (6.69mm). Our novel UVC CNN architecture outperformed the existing Cartesian probability-based algorithm (errors = 4.06mm and 8.07mm for ECGs and EGMs, respectively). Overall, localisation was relatively insensitive to noise and changes in body compositions, however displacements in ECG electrodes and CIED leads caused performance to decrease (errors 16-25mm).
Conclusions. EGM recordings from implanted devices may be used to successfully, and robustly, localize focal VT sources, and aid ablation planning.

Contribution to the field

With this study, we are showing the utility of implanted device electrograms for automating the localisation of focal ventricular tachycardia, with the ultimate aim to aid and improve ablation planning. Moreover, we are showing the power of fast electrophysiological reaction-eikonal simulations in conjunction with torso lead field computations to generate training data for convolutional neural networks, equally important to computational models to allow automated localisation.

Funding statement

Sofia Monaci is funded by the Engineering and Physics Science Research Council (EPSRC; EP/L015226/1). This work was supported by the National Institute for Health Research Biomedical Research Centre at Guy's and St. Thomas' Trust and King's College, the Centre of Excellence in Medical Engineering funded by the Welcome Trust and Engineering and Physical Sciences Research Council (EPSRC; WT 088641/Z/09/Z). The views expressed are those of the author(s) and not necessarily those of the National Health Service, and the National Institute for Health Research, or the Department of Health. M.J.B. is supported by a Medical Research Council New Investigator Grant (MR/ N011007/1).

Ethics statements

Studies involving animal subjects
Generated Statement: No animal studies are presented in this manuscript.

Studies involving human subjects
Generated Statement: No human studies are presented in this manuscript.

Inclusion of identifiable human data
Generated Statement: No potentially identifiable human images or data is presented in this study.

Data availability statement

Generated Statement: The raw data supporting the conclusions of this article will be made available by the authors, without undue reservation.

Automated Localisation of Focal Ventricular Tachycardia from Simulated Implanted Device Electrograms: A Combined Physics-AI Approach

Sofia.Monaci[1*], Karli Gillette[2], Esther Puyol-Antón[1], Ronak Rajani[1], Gernot Plank[2], Andrew King[1], Martin Bishop[1]

[1]King's College London, London, United Kingdom

[2]Medical University of Graz, Graz, Austria

*** Correspondence:**
Sofia Monaci
sofia.monaci@kcl.ac.uk

Keywords: Ventricular tachycardia, implanted devices, electrograms, automated localization, torso modelling, deep learning

Abstract

Background. Focal ventricular tachycardia (VT) is a life-threating arrhythmia, responsible for high morbidity rates and sudden cardiac death (SCD). Radiofrequency ablation is the only curative therapy against incessant VT; however, its success is dependent upon accurate localisation of its source, which is highly invasive and time-consuming.

Objective. The goal of our study is, as a proof-of-concept, demonstrating the possibility of utilising electrograms (EGM) recordings from cardiac implantable electronic devices (CIEDs). To achieve this, we utilise fast and accurate whole torso electrophysiological (EP) simulations in conjunction with convolutional neural networks (CNNs) to automate the localisation of focal VTs using simulated EGMs.

Methods. A highly detailed 3D torso model was used to simulate ~4000 focal VTs, evenly distributed across the left ventricle (LV), utilising a rapid reaction-eikonal environment. Solutions were subsequently combined with lead field computations on the torso to derive accurate electrocardiograms (ECG) and EGM traces, which were used as inputs to CNNs to localise focal sources. We compared the localisation performance of a previously developed CNN architecture (Cartesian probability-based) with our novel CNN algorithm utilising universal ventricular coordinates (UVCs).

Results. Implanted device EGMs successfully localised VT sources with localisation error (8.74mm) comparable to ECG-based localisation (6.69mm). Our novel UVC CNN architecture outperformed the existing Cartesian probability-based algorithm (errors = 4.06mm and 8.07mm for ECGs and EGMs, respectively). Overall, localisation was relatively insensitive to noise and changes in body compositions, however displacements in ECG electrodes and CIED leads caused performance to decrease (errors 16-25mm).

Conclusions. EGM recordings from implanted devices may be used to successfully, and robustly, localize focal VT sources, and aid ablation planning.

1 Introduction

Ventricular Tachycardia (VT) is a serious cardiac arrhythmia which represents an important source of morbidity and, upon degeneration into more lethal arrhythmias such as ventricular fibrillation (VF) (Srinivasan and Schilling 2018), sudden cardiac death (SCD) (Harris and Lysitsas 2016; Ritchie and Roser 2018). Hence, the prevention of VT, and its degeneration into VF, is of primary clinical importance to improve morbidity and reduce mortality.

In structurally healthy hearts, VT occurs primarily as a consequence of abnormal ectopic firing in the ventricles, overtaking sino-atrial activation and leading to premature ventricular contractions (PVCs). An effective treatment against ectopic VT is radiofrequency catheter ablation, which aims to target the tachycardia by first locating, and then electrically isolating the region causing the episode. However, procedure success is heavily dependent upon an accurate localization of the VT source. Often, recordings of the focal VT, in the form of an electrocardiogram (ECG) or implanted device electrograms (EGM), exist prior to an ablation procedure, which inherently contain important information related to the focal origin of the VT source. Integration of computational studies and deep learning approaches provides an exciting opportunity to utilise the information contained within these recordings to potentially facilitate automated VT localisation into clinical practice.

In recent decades, computational studies (Trayanova 2011; Clayton and Bishop 2014; Henriquez 2014; Niederer, Lumens, and Trayanova 2019; Yu et al. 2019) have enhanced greatly our knowledge of VT mechanisms and have strengthened diagnostic, therapeutic, and prognostic VT clinical strategies (Niederer, Lumens, and Trayanova 2019; Mendonca Costa et al. 2019; Trayanova et al. 2017; Rantner et al. 2013)**,** helping in the growth of personalised modelling (Medtronic 2016; Prassl et al. 2009; Cedilnik et al. 2018; Potse 2018; Le Bras 2018; Relan et al. 2011). One limitation of the majority of these studies is the dependence on monodomain formulations to represent electric sources in the form of transmembrane voltages. These models are time-consuming, and thus to achieve clinical translation, fast reaction-eikonal (RE) simulations (Neic et al. 2017; Cedilnik, Sermesant, and Sermesant Eikonal 2019) have been the preferred choice. More recently, realistic simulations of full extracellular potentials at specific locations (e.g. ECG electrodes) have been obtained from the combination of lead field (LF) methods (Potse 2018) with fast RE models (Gillette et al. 2021), achieving accuracy comparable to pseudodomain or bidomain formulations, but within a fraction of the computational time.

Using computational simulations of electrophysiological (EP) behaviour has also been exploited to provide training datasets for machine and deep learning algorithms (Yang et al. 2018; Shade et al. 2020); however, these studies did not utilise rapid RE models (Yang et al. 2018; Shade et al. 2020), nor LF methods (Shade et al. 2020). (Yang et al. 2018) was one of the first to utilise convolutional neural networks (CNNs) to localise focal VT sources from simulated ECGs. The novelty of the study was in the integration of computational simulated data with CNN architectures; previous studies had in fact attempted to localise focal VTs from either simulated ECGs - utilising myocardial activation imaging techniques – with no use of artificial intelligence (van Dam, Oostendorp, and van Oosterom 2009) - or from clinical ECGs utilising machine learning algorithms (Zhou et al. 2019).

One important limitation of (Yang et al. 2018) was the restriction of the method to the use of ECGs. Although ECGs are widely used as a routine modality for VT management, they are not always available for VT patients, particularly focal VT patients in which the clinical VT is not inducible. Utilising cardiac implantable electronic devices (CIEDs) EGMs, which the majority of pre-ablation patients have in situ (Pekka Raatikainen et al. 2014; Winterfield et al. 2018), and which continuously

record and store any abnormal arrhythmic activity, could bring great improvements to the automated localisation of focal VT. Recent clinical studies have demonstrated that stored EGM recordings of re-entrant VT episodes from implanted devices can be successfully used to guide the construction of pace-maps during an ablation procedure, with similar accuracy to the use of ECGs, but with the advantage of ensuring the clinical VT is targeted (Yoshida et al. 2010; Yokokawa et al. 2019). In our own recent work, we demonstrated how such EGM recordings might be utilised to perform patient-specific in silico pace-mapping (Monaci et al. 2020), improving pre-procedural ablation planning for complex scar-related VTs. However, literature lacks further investigation on the power of EGM recordings for the localisation of focal VTs, for which computational models can address and answer a variety of different questions, and their use in AI-based algorithms.

In this study, we demonstrate the utility of leveraging the information contained within simulated implanted device EGM recordings for the automated localisation of focal VTs in the LV. This could benefit clinical procedures by providing pre-procedural ablation information of the VT episodes without the necessity of acquiring ECG recordings of the focal VT, which represents the long-term aim of our study. Although the majority of idiopathic VTs originate in the right ventricular outflow track (RVOT) (Srivathsan et al. 2005), focal VTs can also originate from a variety of different locations in the LV (Srivathsan et al. 2005; Yamada et al. 2008; Ito et al. 2003), and automating their localisation could be beneficial to clinical procedures. To achieve our goal, we extend the previous work of (Yang et al. 2018) and utilise fast computational simulations (RE combined with LF) on a realistic image-based torso model to generate ECG and EGM traces, which serve as inputs to a CNN architecture. We show the possibility of obtaining comparable localisation in Cartesian coordinates between ECG-based and EGM-based trained CNNs. Moreover, we show improvement in the overall localisation by introducing a novel CNN algorithm, utilising a local ventricular-specific coordinate system (J. Bayer et al. 2018).

2 Materials and Methods

The workflow of this study is summarized in **Figure 1**. Briefly, this involved using a previously generated 3D torso model (Monaci et al. 2020) (step 1) to rapidly simulate focal pacing across the LV within a RE environment (step 2). These simulated paced beats were combined with LF matrices computed on the standard 12-lead ECG electrodes and manufacturer-guided CIED right (RV) and left (LV) ventricular leads (step 3) to reproduce accurate 12-lead ECG and EGM recordings of the paced beats (step 4). The data were then processed and used as input to an adapted version of a previously developed CNN architecture by (Yang et al. 2018) (step 5) and also to a novel network, consisting of a 2-output regression and a classification CNN (step 6), utilising UVCs, to localise the paced beats (step 7).

2.1 Model Preparation

As in (Monaci et al. 2020), a 3D torso model was generated from a computed tomography (CT) trans-catheter aortic valve implantation (TAVI) panning scan. The torso model included all major organs, with conductivities reported in

Table 1, and a detailed 4-chamber heart, extracted from a separate cardiac CT scan. The patient did not present any visible structural heart disease and consented to the use of their data in ethically approved research: UK Research Ethics Committee reference number 19/HRA/0502 & 15/LO/1803. To decrease computational time without a loss of physiological electric signals, the average ventricular edge length of the biventricular mesh was kept at $738\ \mu m$. Realistic fibre orientation was incorporated into the ventricular myocardium using a well-established rule-based approach (J. D. Bayer et al. 2012).

The LV was geometrically divided into 17 segments, according to the American Heart Association (AHA) guidelines (Selvadurai et al. 2018), as shown in **Figure 2 (A) – (F)**. In addition, each of the segments was subsequently divided into 4, for a total of 68 – **Figure 2 (G) and (H)**. These models were used as guidance for the collection of pacing locations, for the generation of training and testing labels for the existing CNNs, and the visualization of the localized VT sources.

To replicate focal ectopic VTs across the LV segments ~3767 randomly chosen paced beats - single stimuli, with a basic cycle length (BCL) of 400 ms - were simulated using a computationally efficient RE formulation (Neic et al. 2017) within the Cardiac Arrhythmia Research Package (CARP) (Vigmond et al. 2003), utilising the ten Tusscher ventricular cell model (ten Tusscher et al. 2004). Intra- and extracellular tissue conductivities were tuned to achieve physiological QRSs (Costa et al. 2013), comparable to equivalent pseudo bidomain simulations on a higher-resolution mesh (Monaci et al. 2020). Intra- and extracellular conductivities were $0.1845\,S/m$ and $0.6628\,S/m$ along the fibre direction, respectively, and $0.0493\,S/m$ and $0.1769\,S/m$ transverse to it. The corresponding RE conduction velocities (CVs) were $0.5455\,m/s$ and $0.1802\,m/s$, along and transverse the fibre direction respectively.

To allow the computation of extracellular potential signals from specific locations within the torso **Figure 3**, the simulated cardiac potentials of each paced beat were combined with the LF Method (Potse 2018). Specifically, LF matrices were calculated within CARP (Vigmond et al. 2003) on the standard ECG lead locations, and on the RV and LV lead sensing parts of a standard Boston Scientific implanted device (Antoniadis et al. 2017). This virtual device had a non-septal RV lead, with a superior vena-cava (SVC) coil in the right atrium (RA), and a straight LV lead through the coronary sinus, with four sensing LV tips distanced equally at 7.5 mm. Configurations of both 12-lead ECG and CIED are shown in **Figure 4 (A) – (D)**. All sensing electrodes, including the can of the implanted device (CAN), were approximated to single points, to increase the speed of LF computations and subsequent simulations. The computation of these matrices was only performed once for each torso configuration and took ~ 8 minutes (128 cores). Their combination with the RE solutions produced high-fidelity 12-lead ECGs and EGM traces (**Figure 4 (E) and (F)**) in ~ 20 seconds (256 cores) for each paced location. 8 EGM vectors were chosen as the main EGM signals (Monaci et al. 2020), and included far field CAN-SVC, CAN-RV, SVC-RV, and near field RV tip-RV ring and each LV tip-RV tip. However, importantly, additional vector combinations (4 for ECGs and 8 for EGMs) were added to the standard signals to facilitate integration into the CNN algorithms (see Section **2.4**).

Finally, a standardised Universal Ventricular Coordinate (UVC) system was computed on the biventricular mesh (J. Bayer et al. 2018) to facilitate the development of a novel CNN specific to the ventricles, which should be advantageous as it identifies and constrains the localisation of the paced beats inherently within the myocardium. As shown in **Figure 5,** UVCs describe the biventricular mesh using three parameters: z – normalised distance between apex (0) and base (1) along the long-axis - ρ – normalised distance between endocardial (0) and epicardial (1) surfaces along the short-axis - and φ – rotational distance from LV septum.

2.2 CNN architectures

In this study, we developed two separate 2D CNN architectures, which used the same ECG and EGM traces as inputs to identify the location of a simulated paced beat (representing an ectopic VT). The first architecture, based on (Yang et al. 2018), locates the origin of the paced beat in Cartesian coordinates, after converting the outputs of the CNNs. The second utilises a regression and a

classification CNN to locate the VT in UVC space, naturally constraining the final localisation of the focal VT source to the myocardium.

The existing Cartesian probability-based architecture was reproduced from (Yang et al. 2018) and comprised of two classification CNNs – named *Segment* and *EpiEndo* CNNs. *Segment* CNN classified in which LV segment the pacing beat originated, whereas *EpiEndo* CNN determined whether the pacing was endocardial or epicardial (binary decision). In our study, we developed two separate *Segment* CNNs: one classified between 17 LV segments (CNN with 17 output neurons), the other between 68 LV segments (68 output neurons). Briefly, the structure of both *Segment* and *EpiEndo* CNNs consisted of two hidden layers alternating with two pooling layers and terminating with a fully connected (FC) layer. The output of both *Segment* and *EpiEndo* CNNs was a probability distribution (likelihood of each output neuron being the correct class). These distributions were obtained utilising a softmax function on the output of the final FC layer. As performed in (Yang et al. 2018), the probability distributions (P^i_{seg} and $P^j_{epiendo}$ for *Segment* and *EpiEndo*, respectively) of each output segment (largest probability) and its adjacent segments were then combined with the centres of gravity $CoG(x,y,z)ij$ of the corresponding endocardial and epicardial surfaces, as shown in **Eq. 1,** to localise a paced beat in Cartesian coordinates.

$$(S_{cartesian})_{out} = \sum_{i=1}^{N} P^i_{seg} \times \left(\sum_{j=1}^{2} P^j_{epiendo} \times CoG(x,y,z)ij \right) \quad \textbf{Eq. 1}$$

The distance of the localised sources to the ground truths (simulated sources) was expressed in terms of localisation errors (computed as Euclidean distance in *mm*).

Our novel UVC-based algorithm is comprised of one regression CNN, outputting z and ρ, and one 68-feature classification CNN, predicting the rotational coordinate φ. The structure of both CNNs was similar to the Cartesian probability-based network (hidden layer – hidden layer – pooling layer – FC layer), as shown in **Figure 6**. Because of the cyclic nature of φ, a three-output regression would have not returned satisfying and accurate results; hence, we used φ to divide the LV into 68 "wedges" (φ was grouped into intervals of 0.09 radians with each class assigned a label from 1-68, spanning $\varphi = -\pi$ to $\varphi = \pi$). Using a higher number of LV "wedges" would have not returned desirable accuracies, thus we decided to use a number of features (68) that had worked for *Segment* CNN and that was still suitable for achieving precise localisation along φ. For the final localisation of the paced beats, the outputs of the 68-feature classification ("wedges" with the highest probabilities) were converted back to φ, and combined with z and ρ regression predictions.

Both Cartesian probability-based and UVC-based algorithms were implemented in Python using Scikit-learn (Pedregosa et al. 2011) and TensorFlow (Abadi et al. 2015).

2.3 CNN Localisation performance

Localisation performance of the Cartesian probability-based algorithm was expressed in terms of localisation error in mm, as described above**.** The same metric was used for our novel UVC-based architecture, however the predicted values were first transformed from UVC space to Cartesian space (by locating the closest node in the mesh, with appropriate scaling of UVC coordinates (J. Bayer et al. 2018)), and then the distance with the ground truths (simulated pace beats) was evaluated (Euclidian distance, in mm).

For the *Segment* CNN of the Cartesian probability-based architecture, testing performance was evaluated in terms of accuracy, to allow comparison with results from (Yang et al. 2018). Accuracy is defined as the percentage of paced beats correctly classified within each segment.

2.4 CNNs Training and Testing

Training and testing inputs of both Cartesian probability-based and UVC-based CNNs were ECG and EGM traces computed from 3767 pacing excitations across the LV. To facilitate the execution of the 2D CNNs, the ECG and EGM signals had to be placed in square matrices; hence, we added 4 additional leads to the standard 12-lead ECGs (LL-RA-LA, LA-RA-LL, RA-LA-LL, (RA+LA+LL)/2), as performed in (Yang et al. 2018), and 8 more EGM vectors to the standard 8 EGMs (CAN-each LV tip, SVC-each LV tip), to achieve a total of 16 combinations of ECG and EGM vectors. QRSs were then extracted and sampled in time (16 time points), and stacked in 16x16 matrices, as shown in **Figure 4 (E) and (F)**. 2767 sets of these ECG and EGM matrices were used for training, and were uniformly distributed across the myocardium (~36% intramural/mid-wall, ~32% epicardial, and ~32% endocardial), with the exception of *EpiEndo* training data which was epicardial and endocardial only (Yang et al. 2018). White Gaussian noise with a signal-to-noise ratio (SNR) of 25db was then added ten consecutive times to all 16 ECG and EGM leads of the training set to augment the data by ten-fold (~ 27670), and increase robustness of the CNN training. A ten-fold cross validation was performed in the existing Cartesian probability-based CNNs as part of the training (Yang et al. 2018), with a 90% (training) -10% (validation/testing) split. On the other hand, the cross validation was used for hyper-parameter tuning in the UVC-based networks. After training, the localisation performance of both Cartesian probability-based and UVC-based networks was tested by feeding the retained 1000 sets of ECG and EGM QRSs, with a SNR of 25db. Parameters of both *Segment* and *EpiEndo* CNNs were taken from (Yang et al. 2018); batch size was set to 23, number of epochs to 10, learning rate to 0.001 and cross-entropy was used as loss function. A ReLU function was used as the activation function for feed-forward propagation, and a gradient-descent-projection method as the back propagation algorithm. In our UVC-based networks, we used similar parameters, except for the regression where we set the batch size to 23, the number of epochs to 15 and we used mean absolute error as loss function.

2.5 Investigation of model uncertainties

Localisation performance of both Cartesian probability-based and UVC-based CNN architectures, trained on the data described above, was also investigated by introducing different noise levels to the retained 1000 sets (SNR = 5db, 10db, 15db, 20db and 30db). Moreover, we investigated the localisation performance of both architectures as body compositions of the torso model were also varied, shown in **Table 2**, as well as different ECG electrodes configurations (**Figure 7**) and different CIED configurations (**Figure 8).** For all these variations, LF matrices were recomputed (according to the new organ conductivities or electrodes positions) and combined with the retained 1000 intramural excitations to obtain new ECG and EGM matrices. These traces were then used to test both previously-trained CNN architectures. Some of the major organ conductivities were varied according to physiological variations (Sovilj et al. 2014; Trakic et al. 2010); however, we chose to pair specific changes (for instance, liver and lungs, fat/muscle, named "bath", and liver, different blood pools, etc.) to challenge CNN localisation performance. ECG electrodes were displaced by 5 cm in all major orthogonal directions, and across all leads. Specifically, we shifted all ECGs leads upwards (**Figure 7 (A)** and downwards **(B)** – RA and LA were always shifted downwards, and LL upwards -, towards the left **(C)** and the right **(D)**. Moreover, in one configuration **(E),** the distance between ECG leads was increased by ~ 10 cm. Finally, we simulated variations in electrode location and diameter of the virtual implanted device, as reported in (Antoniadis et al. 2017) for different cardiac-resynchronization

therapy (CRT-D) devices available in the market. Specifically, we changed the spacing between the sensing electrodes of the straight LV lead, to account for shorter or longer inter-electrode distance; in addition, we increased the diameter of RV and LV tips to ~ 2 mm. In the latter scenario, instead of considering the EGM signals from single point electrodes, we averaged the signals obtained from a cloud of points within a 2 mm radius, to simulate more realistic conditions, and investigate whether our single point approximation of the CIED leads could affect the final localisation. Finally, we considered the case of a septal RV coil configuration, which has been tested in CRT-D (Leclercq et al. 2016) and cardioverter defibrillators (ICD) (Winter et al. 1998).

3 Results

3.1 Utility of EGMs in existing Segment/EpiEndo based CNNs

We successfully reproduced the existing classification CNNs, namely *Segment* and *EpiEndo*, introduced by (Yang et al. 2018), to be trained and tested not only on ECG traces, but also on 16 different combinations of EGM vectors from a standard CIED with RV and LV leads. Testing performance of *Segment* CNN was similar for both ECG-based and EGM-based testing. As shown in **Figure 9 (A),** 86.76% accuracy was achieved for ECG-based testing, and 79.70% for EGM-based testing (SNR = 25db).

The precision of *Segment* CNN in each segment, which defined how correct the CNN is at classifying one segment, is shown in **Figure 9 (B).** Here, we see that ECGs and EGMs have a similar influence on the network in almost every segment, with only few exceptions. The three highest precisions are in segments 1, 10 and 14 for ECG-based testing, and 1, 10 and 16 for EGM-based. The three lowest are in 2, 3 and 15 for ECGs, and 2, 7 and 9 for EGMs.

3.2 Utility of EGMs in Cartesian probability-based Localisation

Localisation in Cartesian space of each paced beat, from either ECG or EGM signals, was possible by combining probability distributions of *Segment* and *EpiEndo* CNNs (as shown in **Eq. 1)**. The localisation performance, defined as the Euclidean distance in mm between an estimated source and the real location of the simulated paced beat, for the testing dataset of 1000 cases, is reported in **Figure 10** for ECG-based and EGM-based testing. ECG-based localisation produced a mean localisation error of 11.76 ± 5.32 mm and 13.25 ± 6.79 mm for EGM-based localisation.

Application of the 68-feature *Segment* CNN, based on the 68-segment LV AHA model shown in **Figure 2 (G)**, was able to reduce localisation errors of both ECGs and EGMs to 6.69 ± 3.19 mm and 8.74 ± 6.41 mm respectively, as shown in **Figure 10**.

3.3 UVC-based Localisation

Further improvements in localisation performance were made by developing two CNNs which returned the position of a paced beat in a reference frame specific to the ventricles (UVCs). This UVC-based localisation outperformed the Cartesian probability-based localisation, as shown in **Figure 11 (A)**, reducing localisation errors to 4.06 ± 2.47 mm and for 8.07 ± 8.26 mm for ECG and EGM-based testing, respectively.

UVC-based localised sources are visualised in 2D in a patient-specific bull's eye diagram, shown in **Figure 11 (B)** for 30 beats, as previously illustrated in **Figure 5.** Here, a paced beat can be visualised using its UVC coordinates, and can be compared to the ground truth, revealing a close match between

all pairs. The radius of the diagram describes the distance of a paced beat to the LV apex (centre of the diagram), relatable to UVC *z*, and its circumferential direction (φ) facilitates the positioning of the beat within a specific segment. The intramural location (ρ) of the beat (how far from the endocardium and/or epicardium) is colour coded.

3.4 Sensitivity to Noise

Overall, localisation was only slightly affected by noise, as seen in **Figure 12 (A)** (ECG-based localisation) and **Figure 12 (B)** (EGM-based localisation). As SNR decreased (increased noise), localisation errors increased only slightly, with one exception (SNR = 5db) where the performance of both UVC-based and Cartesian probability-based localisation was reduced. However, all localisation errors were < 12.5 mm for ECG-based localisation. Moreover, noise seemed to affect EGM-based localisation more than ECG-based localisation.

3.5 Sensitivity to Electrode Locations

Displacements of ECG leads and different CIED configurations did affect the localisation performance of UVC-based and Cartesian probability-based algorithms (errors > ~ 15 mm) for ECG and EGM-based testing, as shown in **Figure 12 (C)** and (**D)** respectively. ECG-based localisation was more affected by displacements away from the heart (> 20 mm) – right and downward shifts. Errors in EGM-based localisation were higher (> 20 mm) when considering longer inter-electrode distance (20 mm) and increased lead surface diameter (2 mm). For UVC-based localisation, a septal RV coil configuration caused errors to increase > 20 mm as well.

3.6 Sensitivity to Tissue Conductivities in Torso Model

A comparison between ECG-based and EGM-based localisation for different body compositions is shown in **Figure 13 (A)** (for UVC-based localisation) and **(B)** (for Cartesian probability-based localisation). ECG-based localisation was only affected by a high increase of fat in the torso bath (scenario 3 and 5) and when the whole torso was simplified to bath and lungs (scenario 7). In those three scenarios, mean localisation errors increased to 17.75 ± 9.88 mm, 20.72 ± 10.99 mm and 14.08 ± 7.38 mm for UVC-based testing respectively, and to 13.01 ± 8.89 mm, 15.07 ± 11.20 mm, and 13.88 ± 8.40 mm for 68-segment Cartesian probability-based testing. Other variations of tissue conductivity did not affect the performance of either algorithm (localisation errors < ~ 8 mm).

Finally, EGM-based testing was less affected by changes in body compositions during Cartesian probability-based localisation. Similar to above for ECG-based localisation, simplification of the torso to bath and lungs (scenario 7) caused the highest mean error (14.83 ± 11.24 mm), but in all other scenarios localisation ranged between 9.04-10.66 mm. On the other hand, UVC-based EGM localisation had a similar trend to ECG-based localisations, with errors > 15 mm for scenario 3,5 and 7.

4 Discussion

In this study, we successfully utilised simulated implanted device EGMs to localise virtual focal VT sources using CNNs, achieving accuracies that could be useful in clinical settings. A previous algorithm (Yang et al. 2018) utilised 12-lead ECGs for a similar purpose; here, we managed to replicate the structure of the CNN architecture for EGM traces and improve the overall localisation by introducing a higher number of segments in the AHA LV model. Moreover, we also improved the overall localisation precision by introducing a novel architecture comprised of regression and

classification algorithms, which was able to identify the source in a framework specific to the ventricles, easily interpretable by clinicians. Finally, we investigated the robustness of both CNN algorithms to the introduction of uncertainties, such as different noise levels in the data, and possible inter-patient variabilities (different body compositions, ECG lead positions, and CIED configurations).

4.1 Successful application of EGMs in existing Cartesian probability-based algorithm

Simulated focal VT sources were successfully identified from 16 combinations of implanted device EGM vectors. In the previous study, (Yang et al. 2018) achieved localisation precision in the range of 10-11 mm when utilising a combination of 16 ECG vectors; here, we reduced localisation errors to 6.69 mm and 8.74 mm for ECG and EGM traces respectively by incrementing the number of segments in the LV to 68. In clinical practice, the average diameters of catheter tips are between 4 mm and 8 mm (Ilg et al. 2010), limiting the average lesion size to a minimum of ~ 8.5 mm (Wittkampf, Hauer, and Robles de Medina 1989). Hence, we achieved localisation precisions in a range suitable for improving ablation planning. Especially in patients with a nonstable condition, pre-planning of these procedures could be expedited and aided if the acquisition of ECG data during VT would not be required, which can be achieved by utilising information stored in implanted devices. Our algorithm thus proposes a first level of investigation that could direct clinicians to the region of interest with high precision. Moreover, we achieved ECG-based and EGM-based testing accuracies in ranges comparable to (Yang et al. 2018) (>77%). Similar patterns to the previous study were seen when investigating how noise affects the localisation; only a loss in accuracy and localisation precision is seen with SNR = 5 db. Interestingly, noise seems to have a greater impact on EGM-based localisation than on ECGs. This could be explained by the fact that implanted device sensing vectors are closer to one another and to the cardiac electrical activity, amplifying variations caused by noise, thus affecting EGM-based localisation to a greater degree.

4.2 Novel UVC-based algorithm improves localisation

Our novel UVC-based algorithm improves localisation to 4.06 mm and 8.07 mm for ECGs and EGMs respectively, outperforming the existing study. Whereas the Cartesian probability-based algorithm relies on combining probabilities of two networks with the geometrical centres of gravity of each LV segment to locate a VT origin, our architecture predicts the actual location of the source in terms of its (normalised) distance from the apex, the LV septum and, most importantly, the endocardium. Furthermore, it intrinsically bounds the localisation to the myocardium. Knowing the exact intramural (mid-wall) location, a VT source could help in the choice of power, tip diameter and lesion size to apply, as well as access direction (epicardial or endocardial), in pre-procedural planning. Finally, our novel localisation facilitates the visualisation of focal estimates, by plotting a patient-specific bull's eye diagram, where the radius represents the distance from the apex and the circumferential direction relates to septal, anterior, inferior and lateral LV segments.

4.3 Automated localisation is only affected by extreme changes in ECG lead positions and implanted device lead configurations

Focal VT localisation is only marginally affected by differences in body compositions. However, to increase the accuracy of the results, a torso model constructed for algorithm training should at least include all major thoracic and abdominal organs with realistic conductivity values; our findings suggest that representing bath and lungs (as used in Yang et al) only produce signals which differ substantially from more complete torso models, importantly affecting localisation accuracy. Moreover, EGM-based algorithms seem to be more robust to tissue variations, possibly due to the closer positioning of the device leads to the electrical cardiac source, with extracellular potentials being less affected by the

surrounding tissue/organ conductivities. Displacements in ECG leads and differences in common CIED configurations do seem to have an impact on the final localisation; this suggests the necessity of integrating a higher variability in the training data, or extrapolating ECG or CIED patient-specific information from imaging data to strengthen future automated algorithms, and allow clinical validation and translation.

4.4 Limitations

A notable limitation of this study is the absence of clinical validation. However, our main goal was to strengthen the automated localisation of focal VTs and investigate properties of our 3D pipeline that need improvement for future clinical studies. For future validation of our in-silico EGM model and corresponding CNN localisation, we will need to generate patient-specific 3D models that have been registered and tuned to the clinical framework used during EP mapping and ablation, collect simulated data on such models for CNN training, and test the latter on clinical EGM recordings of the focal VT(s), and/or paced beats, that have been collected from CIEDs directly or from the latter recording during the mapping. When attempting clinical translation in the future, we will also investigate other aspects of our work regarding patient-specific EP properties that were not taken into consideration in this study. Our model required certain simplifications, such as ruled-based fibres and lack of Purkinje activation, that we believe would not make an impact in the final performance of our algorithms when dealing with focal beats, but that could be useful to take into account for more complex patient-specific approaches. Although our cardiac model was static, we do not believe that the absence of electro-mechanical feedback significantly influenced the final ECG or EGM signals, when considering only QRSs (ventricular activation); many studies have validated static simulated electrograms signals against clinical data (Gillette et al. 2021; Cedilnik et al. 2018; Cardone-Noott et al. 2016), showing that it is not necessary to couple mechanical simulations with EP for these types of problems. Moreover, we only considered single beats originating in the LV. In future studies, it will be worth including focal VTs in the RV, which is a common region of VT especially around the outflow track (RVOT). This could be easily achieved by using the UVC system, that covers the RV, to generate labels and prepare simulations, facilitating both modelling and localisation pipelines. Although we believe that simulating multiple paced beats would not have an impact in the final CNN performance and localisation, it will be necessary to achieve more realistic scenarios, as it can influence the waveforms of ECG and EGM traces. Furthermore, extending the automated localisation of VT to more complex episodes (for instance, in presence of micro re-entries and/or infarction) represents an interest of ours that will be addressed in future studies. The investigation on how different signal uncertainties influence the performance of our CNNs could also be extended to include more complex and realistic ways of adding noise to customise computational models to patient-specific settings (Marcotte et al. 2021; Barone et al. 2020). Another aspect of this study that could be refined is the overall structure of our novel UVC-based architecture; both regression and classification networks were implemented following the structure proposed by (Yang et al. 2018), although some parameters were optimised to fit the new tasks. In future studies, deeper networks could be developed, and different input data shapes could be investigated (e.g. 2D versus 1D). Moreover, to tackle the problem of computational efficiency and decrease even further our simulation time when dealing with more complex arrhythmias, we may investigate the possibility of GPU-based models, which have recently opened new perspectives in terms of real-time, physiologically detailed simulations (Vasconcellos et al. 2020).

5 Conclusions

By integrating fast EP simulations with deep-learning algorithms, we have demonstrated the utility of our in-silico pipeline for the simulations of EGMs stored in implanted devices, which, in addition to

12-lead ECGs, can accurately localise focal VTs. Our novel in-silico automated algorithm, that utilizes a coordinate frame specific to the ventricles, increased localization precision above previous segment-classification approaches, facilitating clinical interpretation. Moreover, we showed the necessity of including more variability in the training data regarding lead positions, and the stability, on the other hand, of the localisation to changes in body compositions.

6 Conflict of Interest

Nothing to Declare.

7 Author Contributions

The work was primarily led by Sofia Monaci. Karli Gillette and Dr. Esther Puyol-Antón were consulted in the initial coding of lead field computations and CNN structure, respectively. Dr Ronak Rajani provided the CT data used for torso model creation. Prof. Gernot Plank was responsible for developing and providing the reaction-eikonal and lead field packages within CARP. Finally, Dr. Andrew King and Dr. Martin Bishop supervised the project, guiding the study design and providing useful insights and feedback on every aspect of the work (from the modelling side to the localisation pipeline and the CNN algorithms).

8 Funding

Sofia Monaci is funded by the Engineering and Physics Science Research Council (EPSRC; EP/L015226/1). This work was supported by the National Institute for Health Research Biomedical Research Centre at Guy's and St. Thomas' Trust and King's College, the Centre of Excellence in Medical Engineering funded by the Welcome Trust and Engineering and Physical Sciences Research Council (EPSRC; WT 088641/Z/09/Z). The views expressed are those of the author(s) and not necessarily those of the National Health Service, and the National Institute for Health Research, or the Department of Health. M.J.B. is supported by a Medical Research Council New Investigator Grant (MR/ N011007/1).

9 References

Abadi, Martín, Ashish Agarwal, Paul Barham, Eugene Brevdo, Zhifeng Chen, Craig Citro, Greg S. Corrado, et al. 2015. "TensorFlow: Large-Scale Machine Learning on Heterogeneous Systems." 2015. tensorflow.org.

Antoniadis, Antonios P., Jonathan M. Behar, Ben Sieniewicz, Justin Gould, Steven Niederer, and Christopher A. Rinaldi. 2017. "A Comparison of the Different Features of Quadripolar Left Ventricular Pacing Leads to Deliver Cardiac Resynchronization Therapy." *Expert Review of Medical Devices* 14 (9): 697–706. https://doi.org/10.1080/17434440.2017.1369404.

Barone, Alessandro, Alessio Gizzi, Flavio Fenton, Simonetta Filippi, and Alessandro Veneziani. 2020. "Experimental Validation of a Variational Data Assimilation Procedure for Estimating Space-Dependent Cardiac Conductivities." *Computer Methods in Applied Mechanics and Engineering* 358 (January): 112615. https://doi.org/10.1016/j.cma.2019.112615.

Bayer, J. D., R. C. Blake, G. Plank, and N. A. Trayanova. 2012. "A Novel Rule-Based Algorithm for Assigning Myocardial Fiber Orientation to Computational Heart Models." *Annals of Biomedical Engineering* 40 (10): 2243–54. https://doi.org/10.1007/s10439-012-0593-5.

Bayer, Jason, Anton J. Prassl, Ali Pashaei, Juan F. Gomez, Antonio Frontera, Aurel Neic, Gernot Plank, and Edward J. Vigmond. 2018. "Universal Ventricular Coordinates: A Generic Framework for Describing Position within the Heart and Transferring Data." *Medical Image Analysis* 45 (April): 83–93. https://doi.org/10.1016/j.media.2018.01.005.

Bras, Alexandra Le. 2018. "3D Virtual Heart to Guide VT Ablation." *Nature Reviews Cardiology* 15 (11): 654. https://doi.org/10.1038/s41569-018-0102-0.

Cardone-Noott, Louie, Alfonso Bueno-Orovio, Ana Mincholé, Nejib Zemzemi, and Blanca Rodriguez. 2016. "Human Ventricular Activation Sequence and the Simulation of the Electrocardiographic QRS Complex and Its Variability in Healthy and Intraventricular Block Conditions." *Europace : European Pacing, Arrhythmias, and Cardiac Electrophysiology : Journal of the Working Groups on Cardiac Pacing, Arrhythmias, and Cardiac Cellular Electrophysiology of the European Society of Cardiology* 18 (Suppl 4): iv4–15. https://doi.org/10.1093/europace/euw346.

Cedilnik, Nicolas, Josselin Duchateau, Rémi Dubois, Frédéric Sacher, Pierre Jaïs, Hubert Cochet, and Maxime Sermesant. 2018. "Fast Personalized Electrophysiological Models from Computed Tomography Images for Ventricular Tachycardia Ablation Planning." *Europace* 20 (suppl_3): III94–101. https://doi.org/10.1093/europace/euy228.

Cedilnik, Nicolas, Maxime Sermesant, and Maxime Sermesant Eikonal. 2019. "Model Personalisation Using Invasive Data to Predict Cardiac Resynchronisation Therapy Electrophysiological Response." https://hal.inria.fr/hal-02368288.

Clayton, R.H H, and M.J J Bishop. 2014. "Computational Models of Ventricular Arrhythmia Mechanisms: Recent Developments and Future Prospects." *Drug Discovery Today: Disease Models* 4. https://doi.org/10.1016/j.ddmod.2014.04.002.

Costa, Caroline Mendonca, Elena Hoetzl, Bernardo Martins Rocha, Anton J Prassl, and Gernot Plank. 2013. "Automatic Parameterization Strategy for Cardiac Electrophysiology Simulations." *Computing in Cardiology* 40 (October): 373–76. http://www.ncbi.nlm.nih.gov/pubmed/24729986.

Dam, Peter M. van, Thom F. Oostendorp, and Adriaan van Oosterom. 2009. "Application of the Fastest Route Algorithm in the Interactive Simulation of the Effect of Local Ischemia on the ECG." *Medical and Biological Engineering and Computing* 47 (1): 11–20. https://doi.org/10.1007/s11517-008-0391-2.

Gillette, Karli, Matthias A.F. Gsell, Anton J. Prassl, Elias Karabelas, Ursula Reiter, Gert Reiter, Thomas Grandits, et al. 2021. "A Framework for the Generation of Digital Twins of Cardiac Electrophysiology from Clinical 12-Leads ECGs." *Medical Image Analysis* 71 (July): 102080. https://doi.org/10.1016/j.media.2021.102080.

Harris, Paul, and Dimitrios Lysitsas. 2016. "Ventricular Arrhythmias and Sudden Cardiac Death." *BJA Education* 16 (7): 221–29. https://doi.org/10.1016/j.ccep.2017.08.004.

Henriquez, Craig S. 2014. "A Brief History of Tissue Models for Cardiac Electrophysiology." *IEEE Transactions on Biomedical Engineering* 61 (5): 1457–65. https://doi.org/10.1109/TBME.2014.2310515.

Ilg, Karl, Timir S. Baman, Sanjaya K. Gupta, Scott Swanson, Eric Good, Aman Chugh, Krit Jongnarangsin, et al. 2010. "Assessment of Radiofrequency Ablation Lesions by CMR Imaging After Ablation of Idiopathic Ventricular Arrhythmias." *JACC: Cardiovascular Imaging* 3 (3): 278–85. https://doi.org/10.1016/j.jcmg.2009.09.028.

Ito, Sachiko, Hiroshi Tada, Shigeto Naito, Kenji Kurosaki, Marehiko Ueda, Hiroshi Hoshizaki, Isamu Miyamori, Shigeru Oshima, Koichi Taniguchi, and Akihiko Nogami. 2003. "Development and Validation of an ECG Algorithm for Identifying the Optimal Ablation Site for Idiopathic Ventricular Outflow Tract Tachycardia." *Journal of Cardiovascular Electrophysiology* 14 (12): 1280–86. https://doi.org/10.1046/j.1540-8167.2003.03211.x.

Leclercq, Christophe, Nicolas Sadoul, Lluis Mont, Pascal Defaye, Joaquim Osca, Elisabeth Mouton, Richard Isnard, et al. 2016. "Comparison of Right Ventricular Septal Pacing and Right Ventricular Apical Pacing in Patients Receiving Cardiac Resynchronization Therapy Defibrillators: The SEPTAL CRT Study." *European Heart Journal* 37: 473–83. https://doi.org/10.1093/eurheartj/ehv422.

Marcotte, Christopher D., Flavio H. Fenton, Matthew J. Hoffman, and Elizabeth M. Cherry. 2021. "Robust Data Assimilation with Noise: Applications to Cardiac Dynamics." *Chaos* 31 (1): 013118. https://doi.org/10.1063/5.0033539.

Medtronic. 2016. "Cardioinsight Mapping Vest ." 2016. https://www.medtronic.com/us-en/healthcare-professionals/products/cardiac-rhythm/cardiac-mapping/cardioinsight-mapping-vest.html.

Mendonca Costa, Caroline, Aurel Neic, Eric Kerfoot, Bradley Porter, Benjamin Sieniewicz, Justin Gould, Baldeep Sidhu, et al. 2019. "Pacing in Proximity to Scar during Cardiac Resynchronization Therapy Increases Local Dispersion of Repolarization and Susceptibility to Ventricular Arrhythmogenesis." *Heart Rhythm* 16 (10): 1475–83. https://doi.org/10.1016/j.hrthm.2019.03.027.

Monaci, Sofia, Marina Strocchi, Cristobal Rodero, Karli Gillette, John Whitaker, Ronak Rajani, Christopher A. Rinaldi, et al. 2020. "In-Silico Pace-Mapping Using a Detailed Whole Torso Model and Implanted Electronic Device Electrograms for More Efficient Ablation Planning." *Computers in Biology and Medicine* 125 (October): 104005. https://doi.org/10.1016/j.compbiomed.2020.104005.

Neic, Aurel, Fernando O. Campos, Anton J. Prassl, Steven A. Niederer, Martin J. Bishop, Edward J. Vigmond, and Gernot Plank. 2017. "Efficient Computation of Electrograms and ECGs in Human Whole Heart Simulations Using a Reaction-Eikonal Model." *Journal of Computational Physics* 346 (October): 191–211. https://doi.org/10.1016/j.jcp.2017.06.020.

Niederer, Steven A, Joost Lumens, and Natalia A Trayanova. 2019. "Computational Models in Cardiology." *Nature Reviews Cardiology* 16 (2): 100–111. https://doi.org/10.1038/s41569-018-0104-y.

Pedregosa, Fabian, Vincent Michel, Olivier Grisel, Mathieu Blondel, Peter Prettenhofer, Ron Weiss, Jake Vanderplas, et al. 2011. "Scikit-Learn: Machine Learning in Python Gaël Varoquaux Bertrand Thirion Vincent Dubourg Alexandre Passos PEDREGOSA, VAROQUAUX, GRAMFORT ET AL. Matthieu Perrot." *Journal of Machine Learning Research*. Vol. 12.

http://scikit-learn.sourceforge.net.

Pekka Raatikainen, M J, David O Arnar, Katja Zeppenfeld, Jose Luis Merino, Francisco Levya, Gerhardt Hindriks, and Karl-Heinz Kuck. 2014. "Statistics on the Use of Cardiac Electronic Devices and Electrophysiological Procedures in the European Society of Cardiology Countries: 2014 Report from the European Heart Rhythm Association." https://doi.org/10.1093/europace/euu300.

Plancke, Anne Marie, Adam Connolly, Philip M. Gemmell, A. Neic, Luke C. McSpadden, John Whitaker, Mark O'Neill, et al. 2019. "Generation of a Cohort of Whole-Torso Cardiac Models for Assessing the Utility of a Novel Computed Shock Vector Efficiency Metric for ICD Optimisation." *Computers in Biology and Medicine* 112 (September). https://doi.org/10.1016/j.compbiomed.2019.103368.

Potse, Mark. 2018. "Scalable and Accurate ECG Simulation for Reaction-Diffusion Models of the Human Heart." *Frontiers in Physiology* 9 (APR). https://doi.org/10.3389/fphys.2018.00370.

Prassl, A.J., Ferdinand Kickinger, Helmut Ahammer, Vicente Grau, J.E. Schneider, Ernst Hofer, E.J. Vigmond, Natalia Trayanova, and Gernot Plank. 2009. "Automatically Generated, Anatomically Accurate Meshes for Cardiac Electrophysiology Problems." *IEEE Transactions on Biomedical Engineering* 56 (5): 1318–30. https://doi.org/10.1109/TBME.2009.2014243.

Rantner, Lukas J., Fijoy Vadakkumpadan, Philip J. Spevak, Jane E. Crosson, and Natalia A. Trayanova. 2013. "Placement of Implantable Cardioverter-Defibrillators in Paediatric and Congenital Heart Defect Patients: A Pipeline for Model Generation and Simulation Prediction of Optimal Configurations." *The Journal of Physiology* 591 (17): 4321–34. https://doi.org/10.1113/jphysiol.2013.255109.

Relan, Jatin, Phani Chinchapatnam, Maxime Sermesant, Kawal Rhode, Matt Ginks, Hervé Delingette, C. Aldo Rinaldi, Reza Razavi, and Nicholas Ayache. 2011. "Coupled Personalization of Cardiac Electrophysiology Models for Prediction of Ischaemic Ventricular Tachycardia." *Interface Focus* 1 (3): 396–407. https://doi.org/10.1098/rsfs.2010.0041.

Ritchie, Hannah, and Max Roser. 2018. "Causes of Death." Our World in Data. 2018. https://ourworldindata.org/causes-of-death.

Selvadurai, Breyoni S.N., Valentina O. Puntmann, David A. Bluemke, Victor A. Ferrari, Matthias G. Friedrich, Christopher M. Kramer, Raymond Y. Kwong, et al. 2018. "Definition of Left Ventricular Segments for Cardiac Magnetic Resonance Imaging." *JACC: Cardiovascular Imaging* 11 (6): 926–28. https://doi.org/10.1016/j.jcmg.2017.09.010.

Shade, Julie K., Rheeda L. Ali, Dante Basile, Dan Popescu, Tauseef Akhtar, Joseph E. Marine, David D. Spragg, Hugh Calkins, and Natalia A. Trayanova. 2020. "Preprocedure Application of Machine Learning and Mechanistic Simulations Predicts Likelihood of Paroxysmal Atrial Fibrillation Recurrence Following Pulmonary Vein Isolation." *Circulation: Arrhythmia and Electrophysiology* 13 (7): 617–27. https://doi.org/10.1161/CIRCEP.119.008213.

Sovilj, Siniša, Ratko Magjarević, Amr Al Abed, Nigel H Lovell, and Socrates Dokos. 2014. "Simplified 2D Bidomain Model of Whole Heart Electrical Activity and ECG Generation." *Measurement Science Review* 14 (3): 136–43. https://doi.org/10.2478/msr-2014-0018.

Srinivasan, Neil T, and Richard J Schilling. 2018. "Sudden Cardiac Death and Arrhythmias." *Arrhythmia & Electrophysiology Review* 7 (2): 111. https://doi.org/10.15420/aer.2018:15:2.

Srivathsan, Komandor, Steven J. Lester, Christopher P. Appleton, Luis R.P. Scott, and Thomas M. Munger. 2005. "Ventricular Tachycardia in the Absence of Structural Heart Disease." *Indian Pacing and Electrophysiology Journal*. Elsevier. https://doi.org/10.1016/b978-1-4377-2029-7.00012-7.

Trakic, A., M. Akhand, H. Wang, D. Mason, F. Liu, S. Wilson, and S. Crozier. 2010. "Computational Modelling of Blood-Flow-Induced Changes in Blood Electrical Conductivity and Its Contribution to the Impedance Cardiogram." *Physiological Measurement* 31 (1): 13–33. https://doi.org/10.1088/0967-3334/31/1/002.

Trayanova, Natalia A. 2011. "Whole-Heart Modeling : Applications to Cardiac Electrophysiology and Electromechanics." *Circulation Research* 108: 113–28. https://doi.org/10.1161/CIRCRESAHA.110.223610.

Trayanova, Natalia A, Farhad Pashakhanloo, Katherine C Wu, and Henry R Halperin. 2017. "Imaging-Based Simulations for Predicting Sudden Death and Guiding Ventricular Tachycardia Ablation." *Circulation: Arrhythmia and Electrophysiology* 10 (7). https://doi.org/10.1161/CIRCEP.117.004743.

Tusscher, K H W J ten, D. Noble, P J Noble, and A V Panfilov. 2004. "A Model for Human Ventricular Tissue." *American Journal of Physiology-Heart and Circulatory Physiology* 286 (4): H1573–89. https://doi.org/10.1152/ajpheart.00794.2003.

Vasconcellos, Eduardo C., Esteban W.G. Clua, Flavio H. Fenton, and Marcelo Zamith. 2020. "Accelerating Simulations of Cardiac Electrical Dynamics through a Multi-GPU Platform and an Optimized Data Structure." *Concurrency Computation* 32 (5): e5528. https://doi.org/10.1002/cpe.5528.

Vigmond, Edward J, Matt Hughes, G Plank, and L.Joshua Leon. 2003. "Computational Tools for Modeling Electrical Activity in Cardiac Tissue." *Journal of Electrocardiology* 36 (December): 69–74. https://doi.org/10.1016/j.jelectrocard.2003.09.017.

Winter, Joachim, John E. Heil, Claudia Schumann, Yayun Lin, Christiana M. Schannwell, Ulrich Michel, Jochen D. Schipke, Hagen D. Schulte, and Emmeran Gams. 1998. "Effect of Implantable Cardioverter/Defibrillator Lead Placement in the Right Ventricle on Defibrillation Energy Requirements. A Combined Experimental and Clinical Study1." *European Journal of Cardio-Thoracic Surgery* 14 (4): 419–25. https://doi.org/10.1016/S1010-7940(98)00215-2.

Winterfield, Jeffrey R., Alexander R. Kent, Edward Karst, Nirav Dalal, Srijoy Mahapatra, T. Jared Bunch, Matthew R. Reynolds, and David J. Wilber. 2018. "Impact of Ventricular Tachycardia Ablation on Health Care Utilization." *Heart Rhythm* 15 (3): 355–62. https://doi.org/10.1016/j.hrthm.2017.10.009.

Wittkampf, F H, R N Hauer, and E O Robles de Medina. 1989. "Control of Radiofrequency Lesion Size by Power Regulation." *Circulation* 80 (4): 962–68. https://doi.org/10.1161/01.CIR.80.4.962.

Yamada, Takumi, H Thomas McElderry, Harish Doppalapudi, Yoshimasa Murakami, Yukihiko Yoshida, Naoki Yoshida, Taro Okada, et al. 2008. "Idiopathic Ventricular Arrhythmias Originating From the Aortic Root Prevalence, Electrocardiographic and Electrophysiologic Characteristics, and Results of Radiofrequency Catheter Ablation." *Journal of the American College of Cardiology* 52 (2). https://doi.org/10.1016/j.jacc.2008.03.040.

Yang, Ting, Long Yu, Qi Jin, Liqun Wu, and Bin He. 2018. "Localization of Origins of Premature Ventricular Contraction by Means of Convolutional Neural Network from 12-Lead ECG." *IEEE Transactions on Biomedical Engineering* 65 (7): 1662–71. https://doi.org/10.1109/TBME.2017.2756869.

Yokokawa, Miki, Hyungjin Myra Kim, Ghaith Sharaf Dabbagh, Konstantinos C Siontis, Sangeeta Lathkar-Pradhan, Krit Jongnarangsin, Rakesh Latchamsetty, Fred Morady, and Frank Bogun. 2019. "Targeting Noninducible Clinical Ventricular Tachycardias in Patients With Prior Myocardial Infarctions Based on Stored Electrograms." *Circulation: Arrhythmia and Electrophysiology* 12 (7). https://doi.org/10.1161/CIRCEP.118.006978.

Yoshida, Kentaro, Tzu Yu Liu, Clayton Scott, Alfred Hero, Miki Yokokawa, Sanjaya Gupta, Eric Good, Fred Morady, and Frank Bogun. 2010. "The Value of Defibrillator Electrograms for Recognition of Clinical Ventricular Tachycardias and for Pace Mapping of Post-Infarction Ventricular Tachycardia." *Journal of the American College of Cardiology* 56 (12): 969–79. https://doi.org/10.1016/j.jacc.2010.04.043.

Yu, Joseph K., William Franceschi, Qinwen Huang, Farhad Pashakhanloo, Patrick M. Boyle, and Natalia A. Trayanova. 2019. "A Comprehensive, Multiscale Framework for Evaluation of Arrhythmias Arising from Cell Therapy in the Whole Post-Myocardial Infarcted Heart." *Scientific Reports* 9 (1): 1–16. https://doi.org/10.1038/s41598-019-45684-0.

Zhou, Shijie, Amir AbdelWahab, John L. Sapp, James W. Warren, and B. Milan Horáček. 2019. "Localization of Ventricular Activation Origin from the 12-Lead ECG: A Comparison of Linear Regression with Non-Linear Methods of Machine Learning." *Annals of Biomedical Engineering* 47 (2): 403–12. https://doi.org/10.1007/s10439-018-02168-y.

9.1 Figure Captions and Tables

Figure 1. Study Workflow. The 3D torso model, generated (step 1) from a CT TAVI planning scan, was utilised to pace the LV from different locations, within a fast RE environment (step 2). These solutions were combined with LF matrices computed (step 3) on the 12-lead ECG electrodes and manufacture-guided CIED leads to generate accurate ECG and EGM traces (Step 4), which were then used as inputs to two CNN architectures, one Cartesian probability-based (step 5) and one novel UVC-based (step 6). Localisation of the paced beats across the LV was then computed (step 7) and compared to the actual locations of the simulated beats.

Table 1. Organ conductivities of our torso model. See also (Plancke et al. 2019)**.**

Organs	***Tissue Conductivities (S/m)***
Lungs	0.0714
Bones	0.05
Skin	0.05
Fat/Muscle	0.24725
Liver	0.1667

Spleen	0.1
Kidneys	0.1667
Aorta	0.6667
Ventricular blood pools	0.6667
Atrial blood pools and walls	0.6667
Pericardium	0.2

Figure 2. Patient-specific LV segment models**.** Generic AHA 17-segment model is shown in (F). The equivalent patient-specific model of the LV mesh is shown in (A), with basal, mid and apical segments illustrated in (B)-(D) respectively. An example of the novel 68-segment model is shown in (H), highlighting the equal division in 4 parts of each 17-segment. (G) shows an example of how segment 1 in our mesh was divided into 4 equal segments.

Figure 3. Example of our simulation pipeline. RE single point excitations were simulated in ~ 3767 different locations across the LV (an example of the activation time map generated for a single such paced beat is shown here in (A)). These solutions were combined with the LF matrices computed on the standard 9 ECG leads (V1-V6, RA, LA, LL), and 9 EGM sensing points (LVtip1-4, RVtip, RVring, RVcoil, SVC and CAN=LA), here shown in b) for LF on V1. The final signals at each lead, shown in (C), were then combined to obtain vector combinations shown **Figure 4 (E)** and **(F)**.

Figure 4. Torso set-up. ECG and CIED configurations are shown in (A) – (D). Example of 16 combinations of pacing signals used for training and testing are illustrated in (E) for ECGs and (F) for EGMs.

Figure 5. Patient-specific bull's eye diagram. 3D Patient-specific 17-segment model in (A) and (B) can be related to the 2D representation in (C) by considering UVC coordinates φ and *z*. Specifically, z (the distance from apex to base), can be linked to the radius of the 2D diagram, as shown, separately for each apical (Za), mid (Zm) and basal (Zb) part of the model. φ is linked to the segments along the spherical axis. The final patient-specific 2D 17-segment can be seen in (D), where the various segments (1 to 17) are illustrated from blue-to-red colour range (mapped from panel (B).

Figure 6. UVC-based CNNs. Structure of 68-feature classification (top) and 2-output regression (bottom)**.**

Table 2. Variations in body compositions. Combinations of different organ conductivities within physiological changes are here reported, used in our CNNs sensitivity analysis.

1. Liver: 0.023 (S/m), Lungs: 0.039 (S/m)
2. Bath: 0.45 (S/m) (pure muscle), Lungs: 0.039 (S/m)
3. Bath: 0.05 (S/m) (pure fat), Lungs: 0.203
4. Liver: 0.2 (S/m), Lungs: 0.039 (S/m)
5. Bath: 0.05 (S/m), Lungs: 0.039 (S/m)
6. Bath: 0.45 (S/m), Lungs: 0.203 (S/m)
7. Bath (all organs except lungs): 0.24 (S/m), Lungs: 0.07 (S/m)
8. Skin: 0.117 (S/m)
9. Atria, Ventricles, Aorta: 0.84 (S/m)

Figure 7. Variations in ECG electrode placements. ECG leads were displaced by ~ 5cm upwards (A), downwards (B), towards the left (C), towards the right (D), and by ~ 10 cm (mixed displacements towards the right and left) (E).

Figure 8. Variations in CIED configurations. Different CIED LV configurations according to different manufactures (Boston Scientific, Livanova, Biotronik and Medtronic) are shown on the top panels. The standard configuration of RV and LV leads is illustrated on the bottom left, and the septal RV coil configuration on the bottom right. The main difference between the various configurations is the inter-electrode distance (reported above the manufactures' names).

Figure 9. Cartesian probability-based CNN performance. Testing performance of 17-feature Segment CNN is here reported in terms of accuracy (%) (panel (A)), and precision (panel (B)) for each 17 segment of the LV mesh. ECG-based and EGM-based testing performances are reported in blue and red, respectively.

Figure 10. Localisation performance of Cartesian probability-based algorithm. Localisation errors in mm are reported for ECG-based (blue) and EGM-based (red) testing. A comparison in localisation performance between different *Segment* CNNs can also be seen; 17-feature *Segment* CNN are on the left and 68-feature *Segment* CNN on the right.

Figure 11. Localisation comparison between UVC-based and Cartesian probability-based algorithms. Mean localisation errors (A) are reported in mm with corresponding standard deviations for ECG-based (blue) and EGM-based (red) testing. An example of how VT focal origins compare to UVC-based localised sources is shown in (B); diamonds represent the ground truths, whereas the circles are the CNN outputs. The grey colourbar represents the distance from endocardial (black) to epicardial (white) surfaces of each source, whereas the blue-to-red colourbar represents 1-17 patient-specific AHA segments.

Figure 12. Localisation comparison between UVC-based (light grey) and Cartesian probability-based (dark grey) networks. Localisation performance for ECG-based and EGM-based testing are here reported during sensitivity analysis for different noise levels - (A) and (B) respectively -, and for different lead configurations - (C) and (D) respectively. For all panels, mean errors with corresponding standard deviations are reported for UVC-based (light grey) and Cartesian probability-based (dark grey) localisation. Displacements of ECG leads, shown in **Figure 7**, results in localisation errors in (C); on the other hand, different CIED configurations, shown in **Figure 8**, return errors in (D). Little difference in localisation is present between the two networks with similar mean localisation errors.

Figure 13. Localisation sensitivity to tissue conductivities**.** Mean localisation errors are here reported for UVC-based (A) and Cartesian probability-based (B) localisation as different organ conductivities were changed in the torso model – see **Table 2**. Small differences are seen between ECG-based (red) and EGM-based (blue) localisation errors.

Figure 1.JPEG

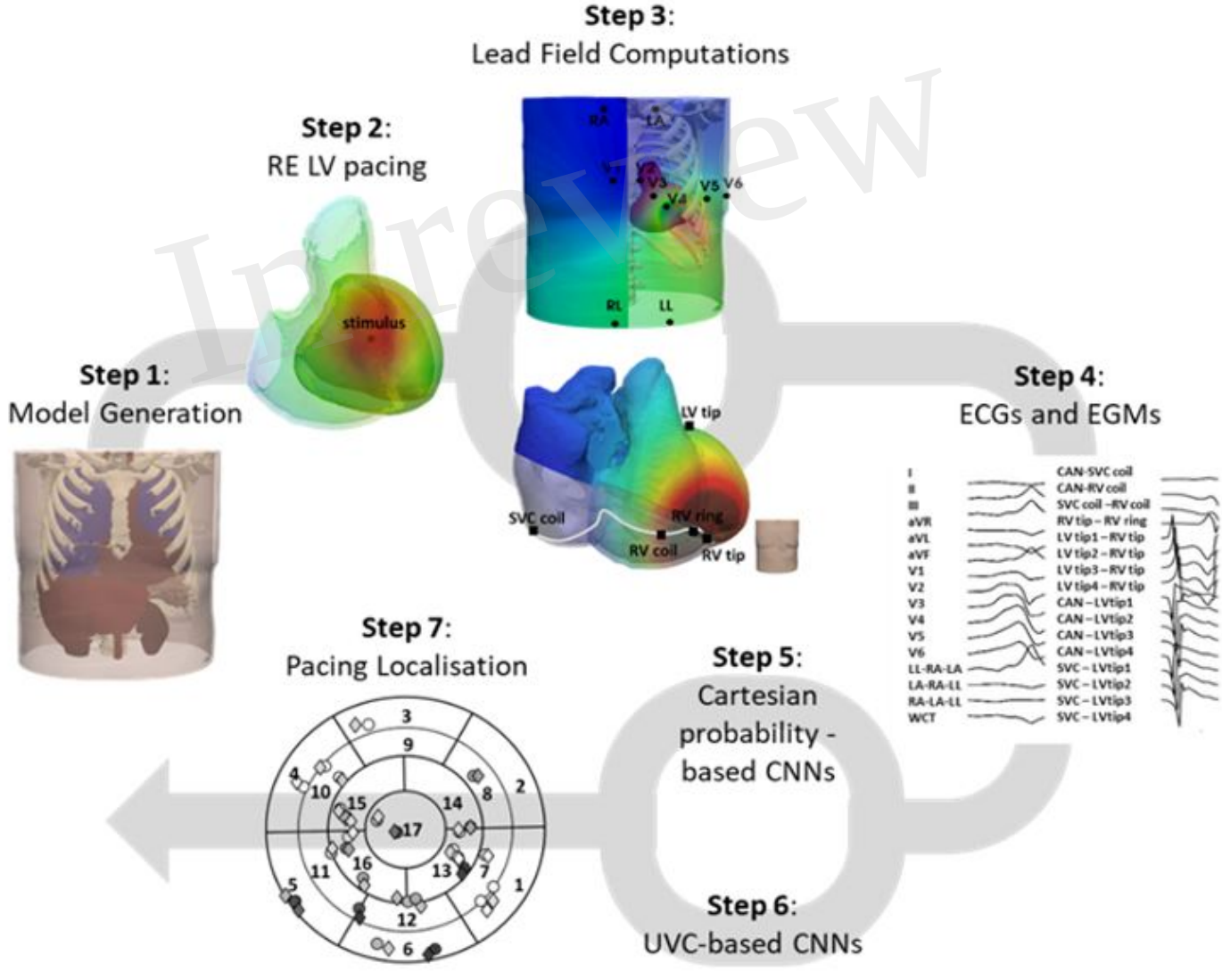

Figure 2.JPEG

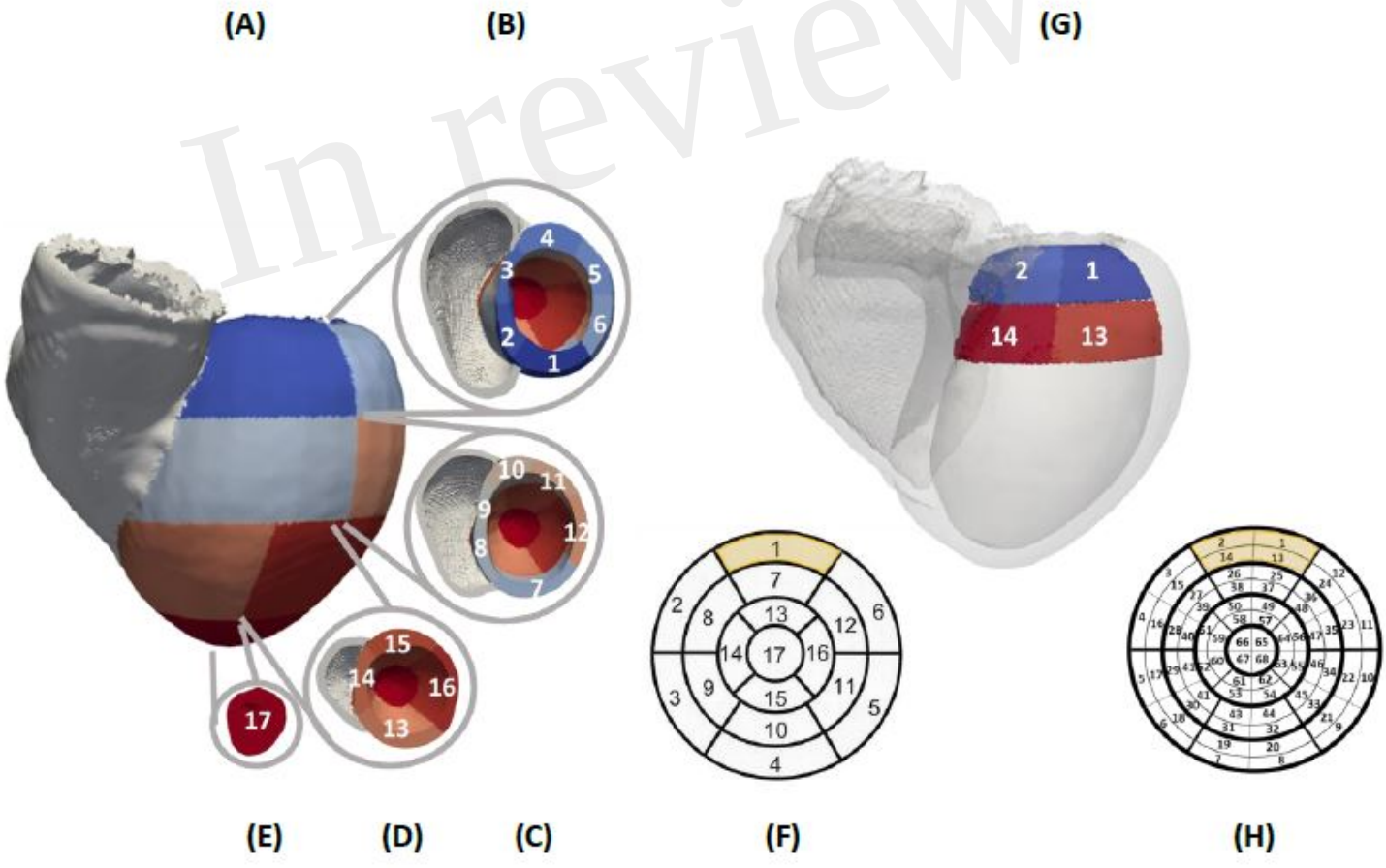

Figure 3.JPEG

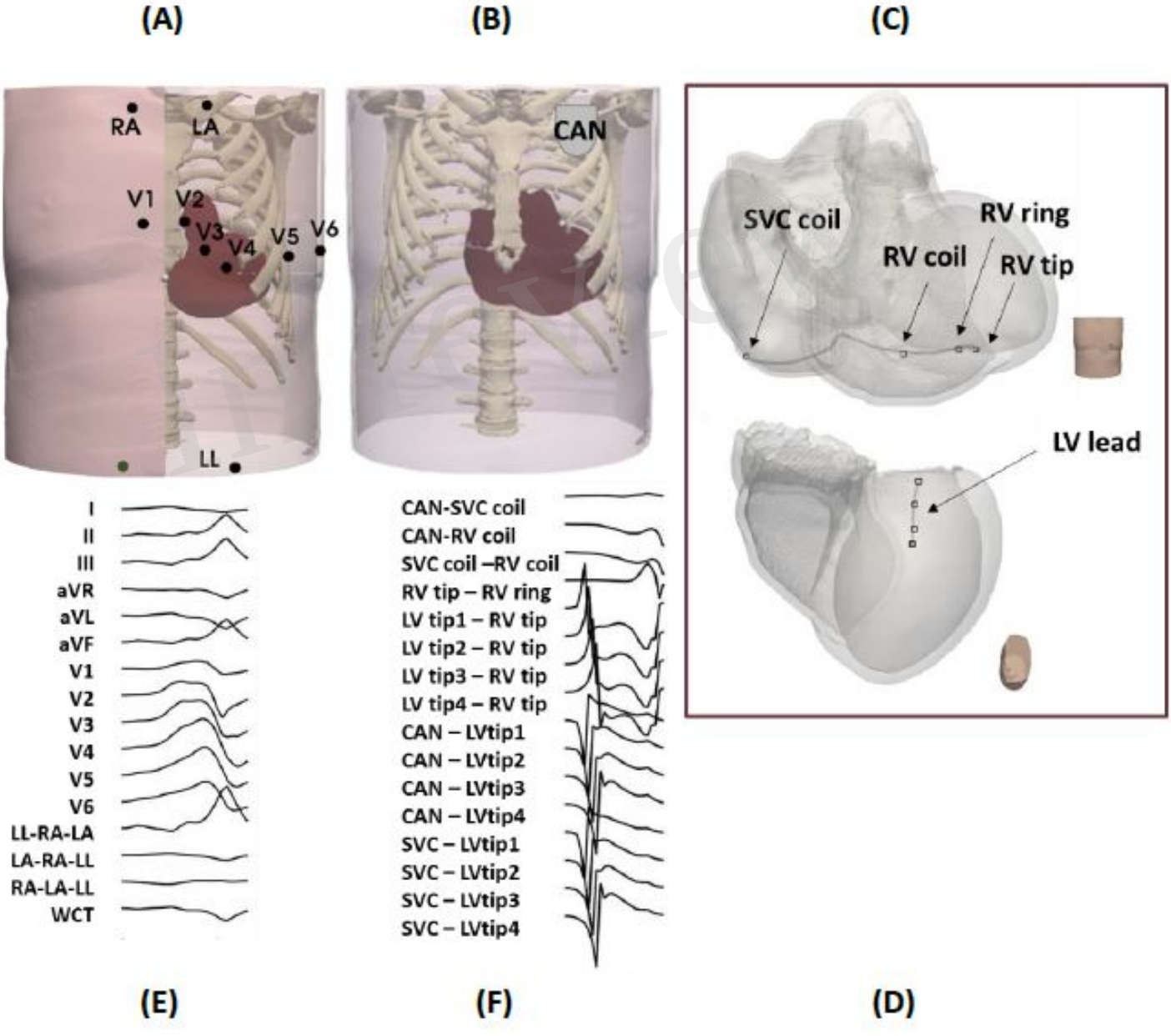

Figure 4.JPEG

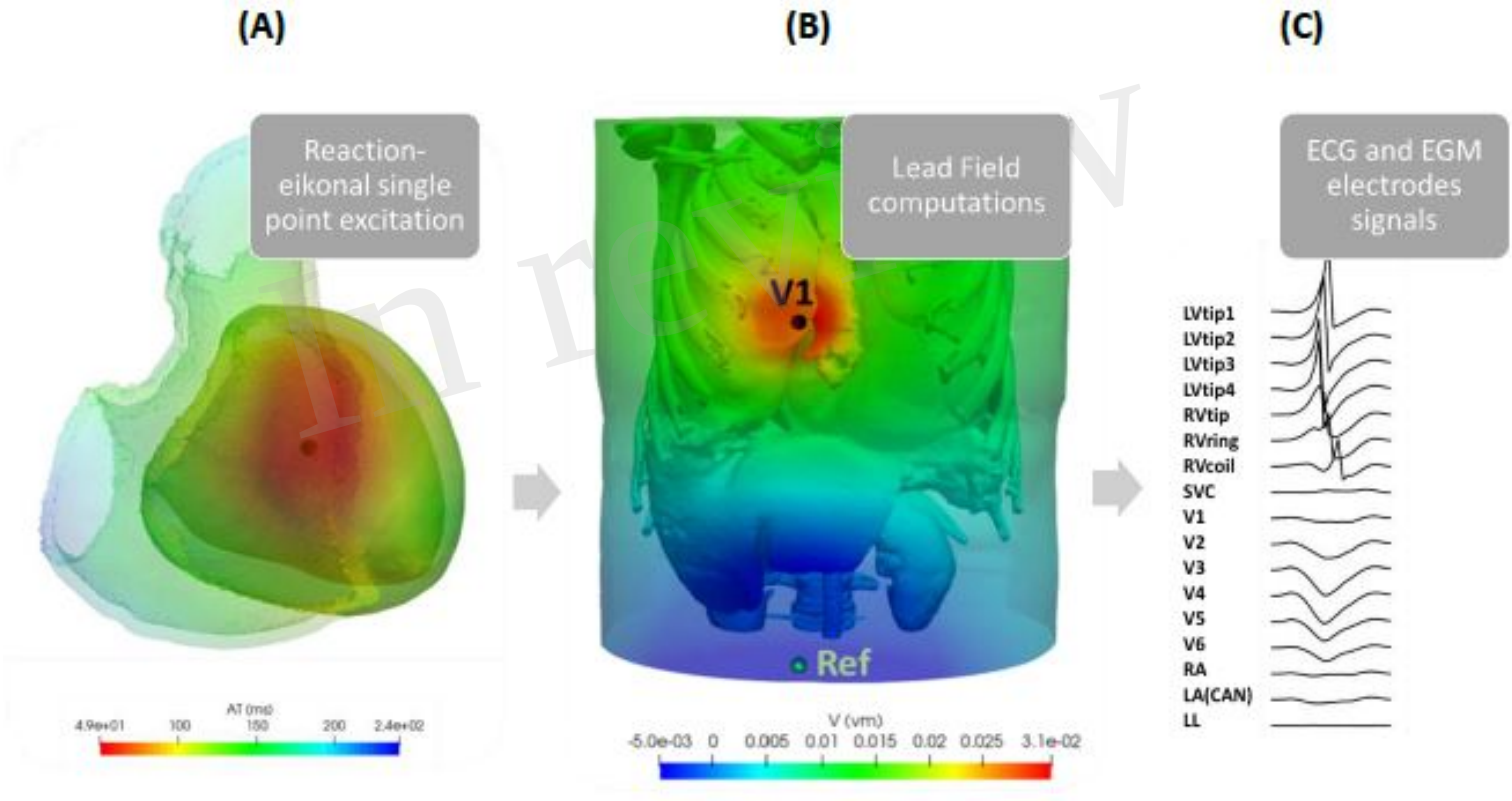

Figure 5.JPEG

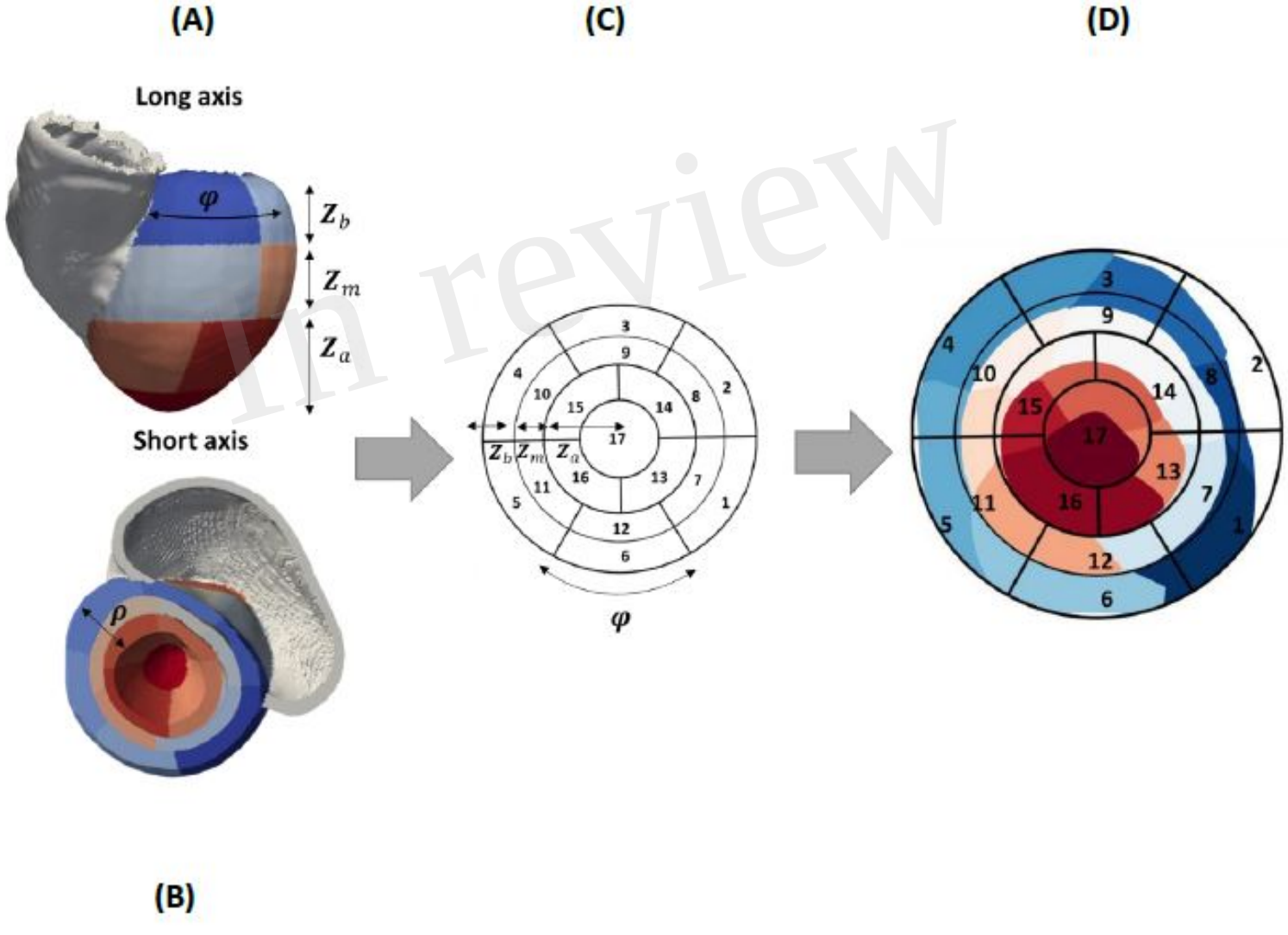

Figure 6.JPEG

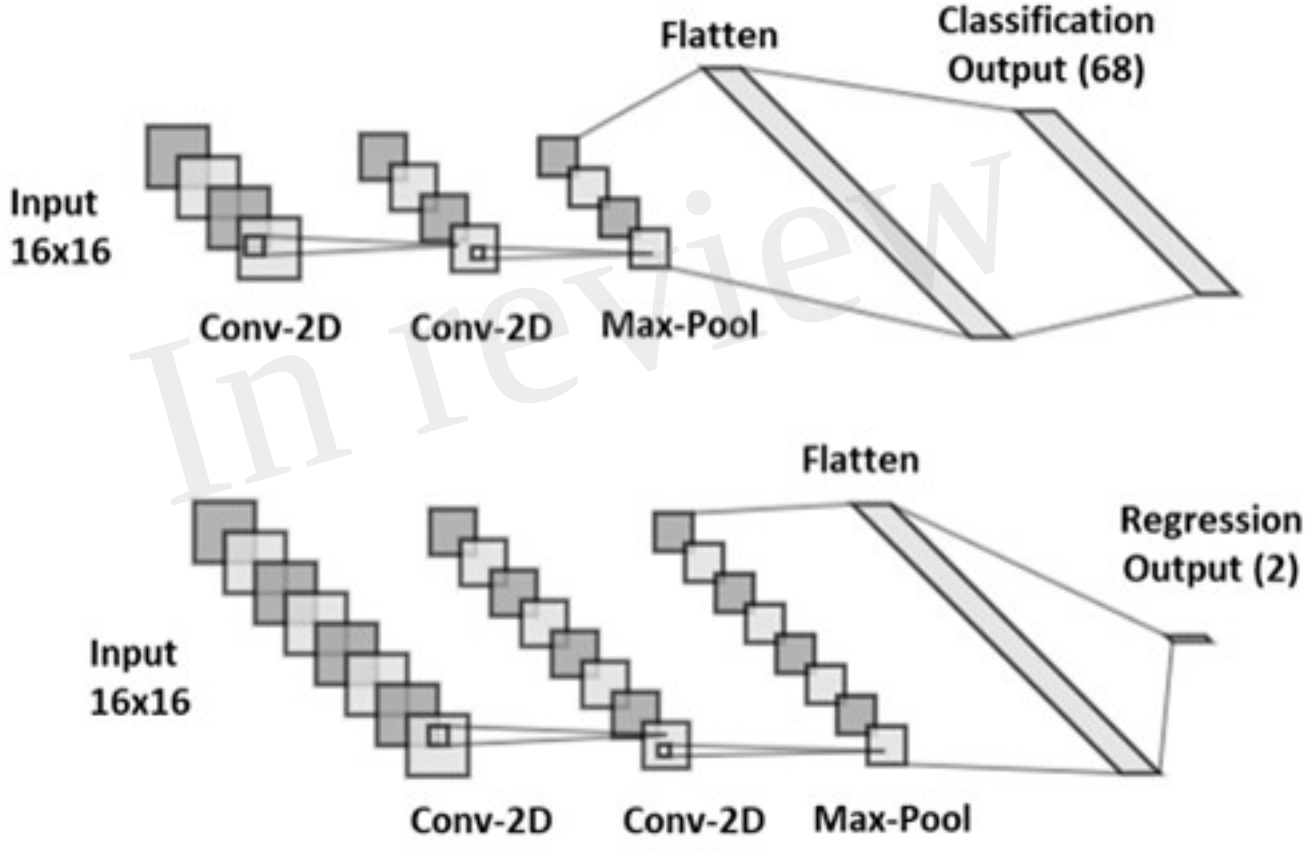

Figure 7.JPEG

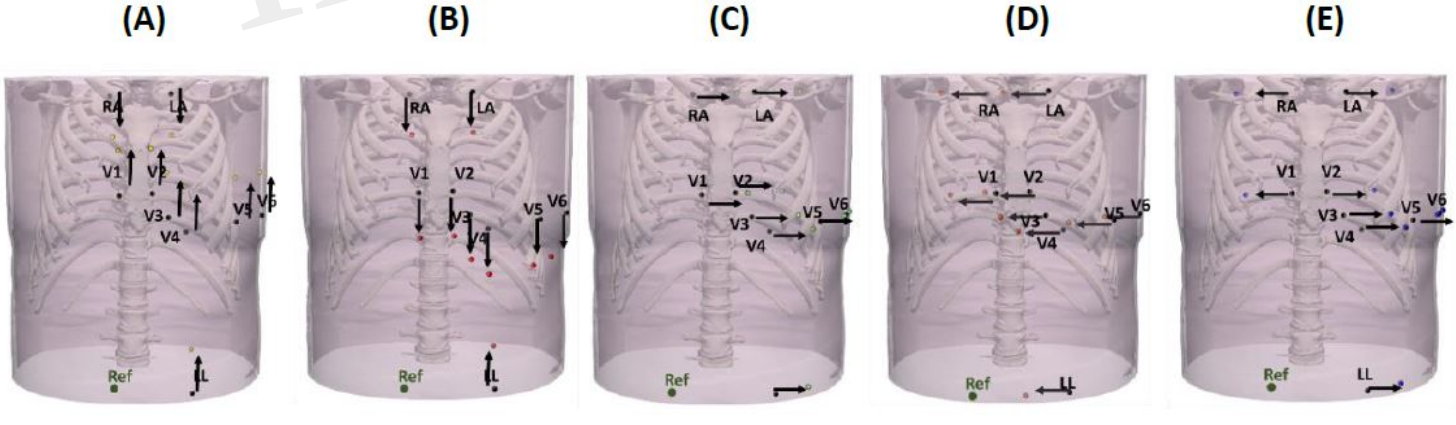

Figure 8.JPEG

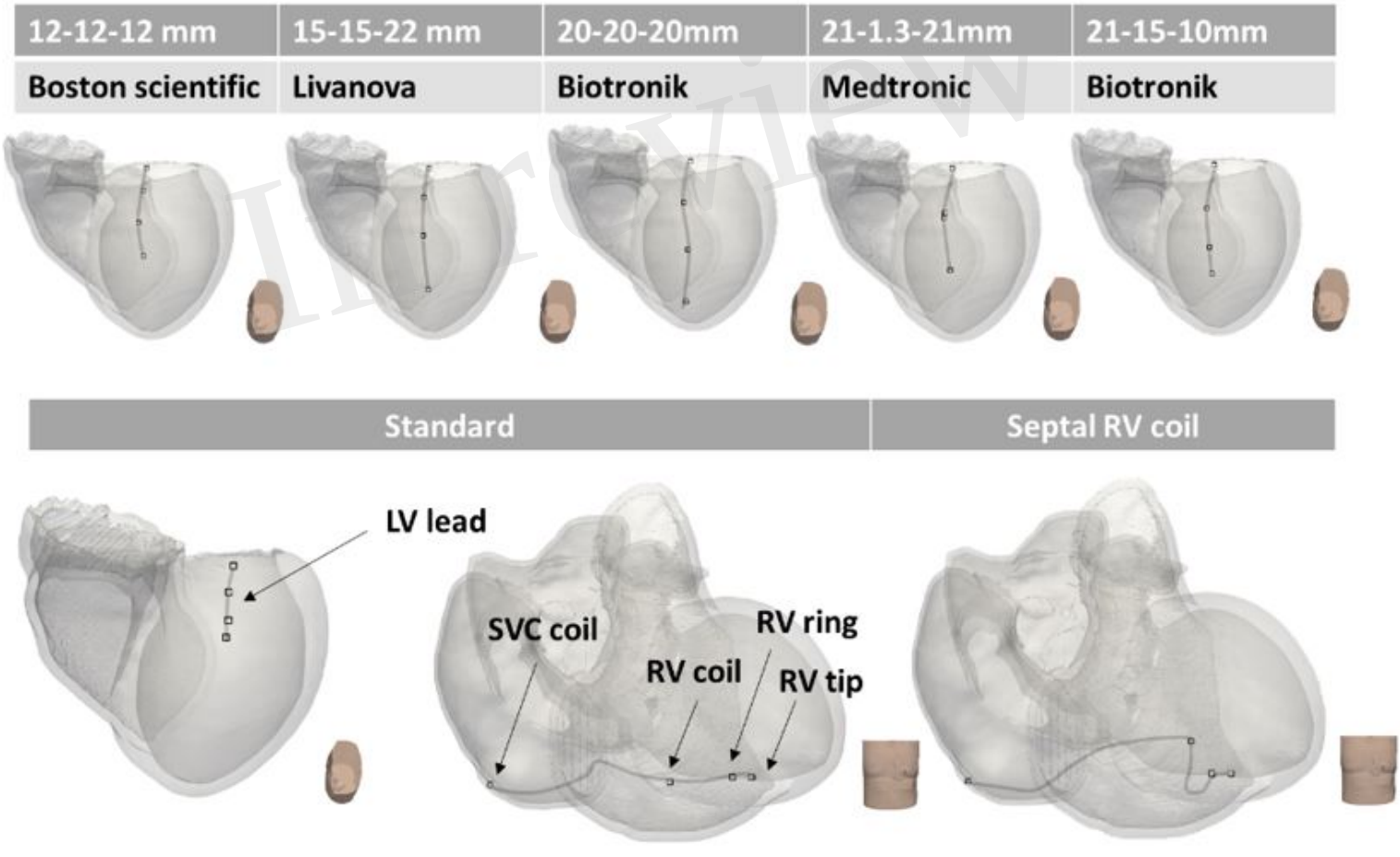

Figure 9.JPEG

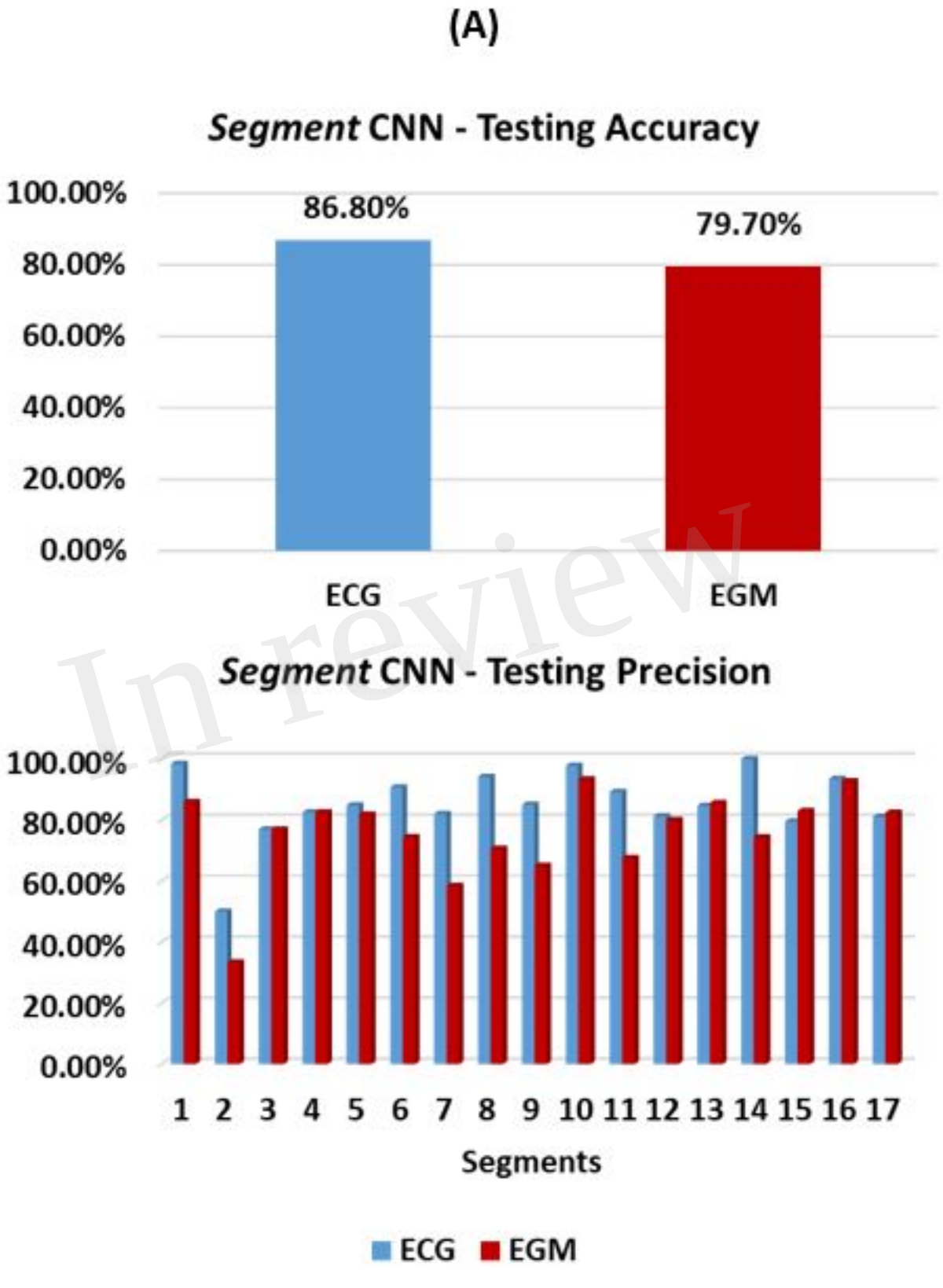

Figure 10.JPEG

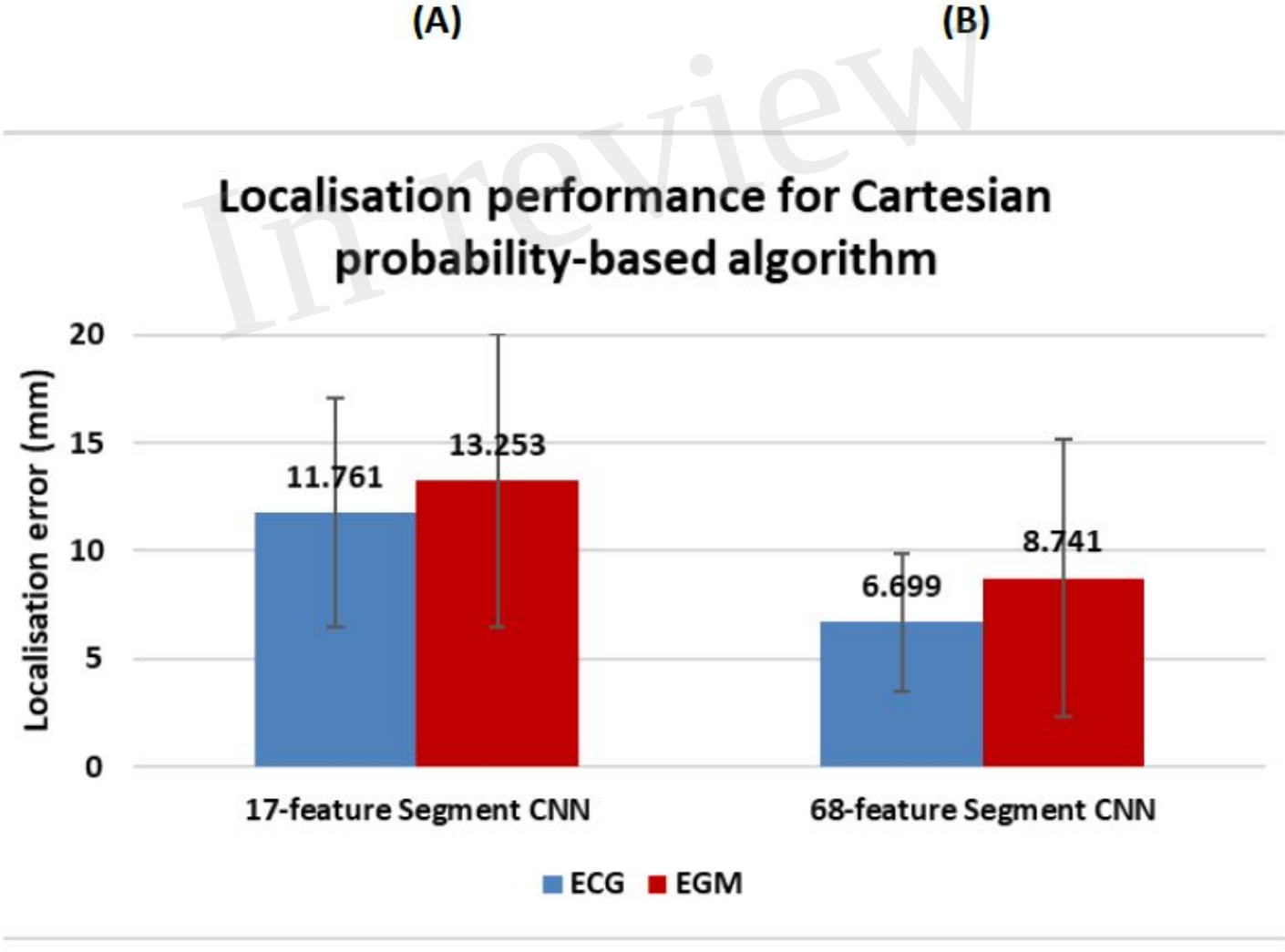

Figure 11.JPEG

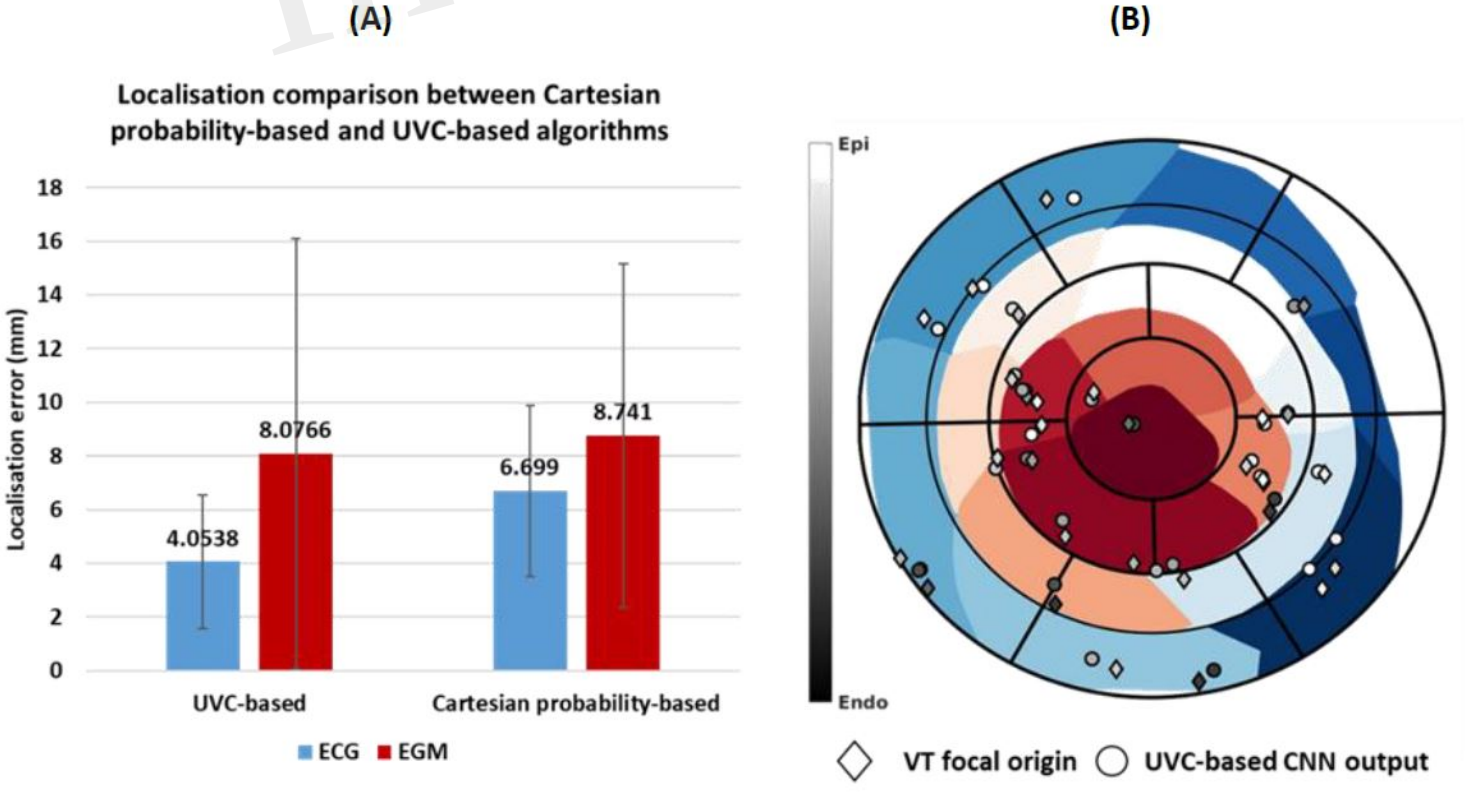

Figure 12.JPEG

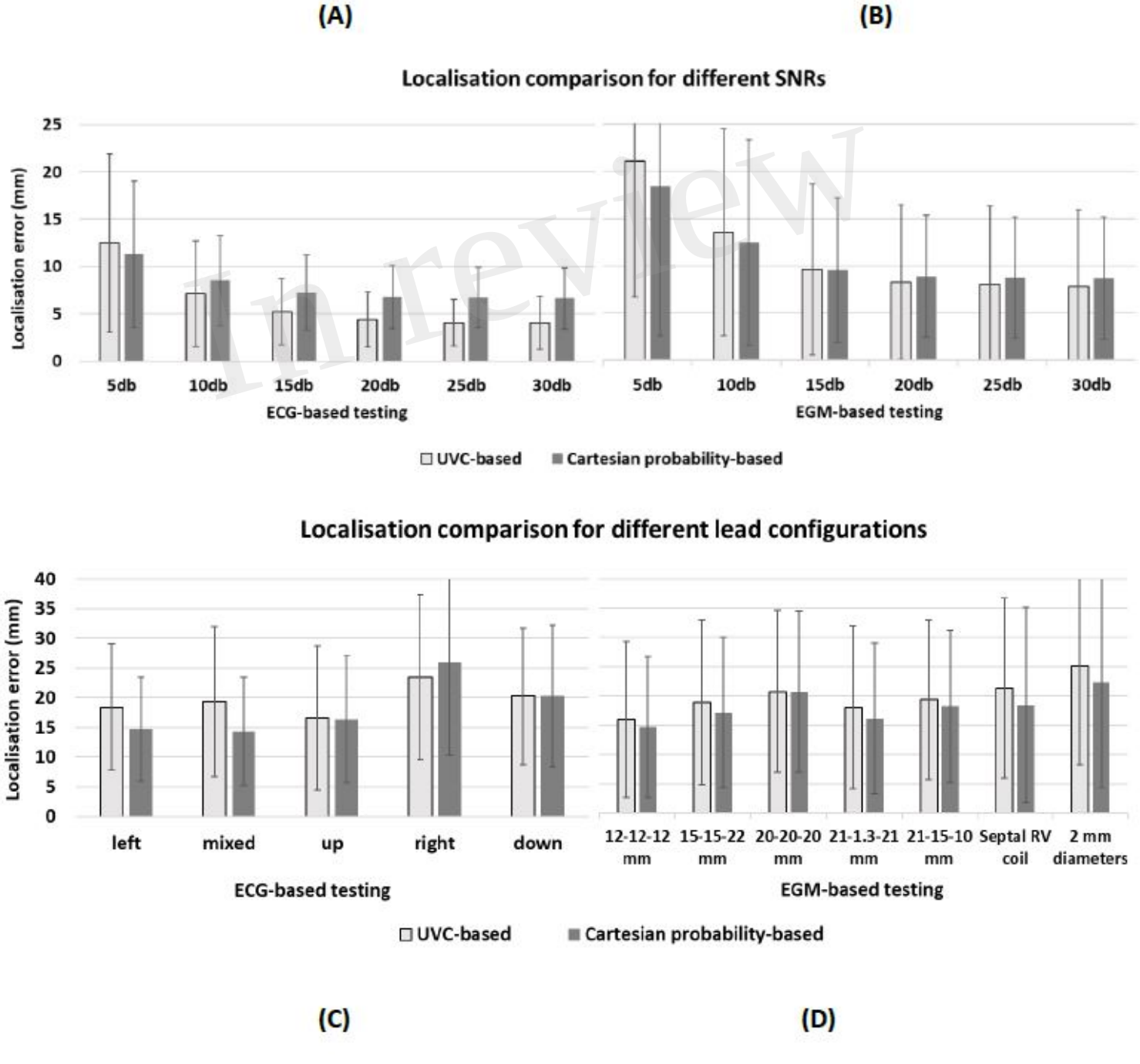

Figure 13.JPEG